# Forced vibroacoustic response of a cylindrical shell in an underwater acoustic waveguide

Jamie Kha, Mahmoud Karimi, Laurent Maxit, Alex Skvortsov, Ray Kirby

▶ **To cite this version:**

Jamie Kha, Mahmoud Karimi, Laurent Maxit, Alex Skvortsov, Ray Kirby. Forced vibroacoustic response of a cylindrical shell in an underwater acoustic waveguide. Ocean Engineering, 2023, 273, pp.113899. 10.1016/j.oceaneng.2023.113899 . hal-04001785

**HAL Id: hal-04001785**
**https://hal.science/hal-04001785**

Submitted on 23 Feb 2023

**HAL** is a multi-disciplinary open access archive for the deposit and dissemination of scientific research documents, whether they are published or not. The documents may come from teaching and research institutions in France or abroad, or from public or private research centers.

L'archive ouverte pluridisciplinaire **HAL**, est destinée au dépôt et à la diffusion de documents scientifiques de niveau recherche, publiés ou non, émanant des établissements d'enseignement et de recherche français ou étrangers, des laboratoires publics ou privés.

# Forced vibroacoustic response of a cylindrical shell in an underwater acoustic waveguide

Jamie Kha[a,*], Mahmoud Karimi[a], Laurent Maxit[b], Alex Skvortsov[c] and Ray Kirby[a]

[a]Centre for Audio, Acoustics and Vibration, University of Technology Sydney, Sydney 2000, NSW, Australia
[b]Univ Lyon, INSA-Lyon, Laboratoire Vibrations-Acoustique (LVA), Villeurbanne Cedex F-69621, France
[c]Maritime Division, Defence Science and Technology Group, Melbourne 3000, Victoria, Australia

ARTICLE INFO

*Keywords*:
Fluid-loaded cylindrical shell
Forced vibroacoustics
Underwater acoustic waveguide
Analytical modeling

ABSTRACT

An analytical approach is proposed to analyze vibroacoustics of an infinitely long thin cylindrical shell under line-distributed harmonic excitation immersed in an underwater waveguide formed by a free surface and a rigid floor. Equations of motion of the thin shell are modeled using Flügge's shell theory, the fluid-structure coupling is implemented with the image source method to account for the infinite reflections of acoustic waves off the waveguide boundaries and Graf's addition theorem is used to reconcile the coordinate systems of the image sources in the analytical expressions. The vibroacoustic response from the proposed analytical model is verified by numerical results obtained from a finite element model, showing excellent agreement. The analytical approach provides a computationally efficient tool for parametric investigation into the relative effects of the proximity of the free surface and/or rigid floor on the vibroacoustic behavior of the shell.

## 1. Introduction

Investigations of submerged cylindrical shells are of ongoing relevance due to the application to analysis of marine engineering systems such as underwater vehicles, submerged pipelines and subsea pile driving. The vibroacoustic analysis of such systems can be performed using element-based methods such as finite element method (FEM) and/or boundary element method (BEM), which involves solving a numerical discretization of the fluid-structure model. However, to accurately solve a vibroacoustic system, these methods require long simulation run times and large data storage requirements. Moreover, the computational cost of simulations increases at higher frequencies as more elements are needed to resolve the structural and acoustic waves. Hence, these methods are used for low frequency analysis. Although analytical solutions are very difficult to obtain and are limited to simple geometries, they provide an efficient tool for performing parametric studies in a wider frequency range.

Thin infinite cylindrical shells offer a simplification to the marine engineering systems, as there are various thin shell theories that have been developed and offer simple analytical developments. Infinite cylindrical shells under line-force distributed loads can be used for efficient and approximate investigations by employing longitudinal symmetry. To date, vibroacoustic studies of infinite cylindrical shells in literature have been analytically and numerically carried for an infinite fluid domain (Junger and Feit, 1986; Pathak and Stepanishen, 1994; Guo, 1996; Liu et al., 2010; Kerferd et al., 2020; Maxit et al., 2020a,b; Williams et al., 2022), semiinfinite fluid domain (Salaün, 1991; Ergin and Temarel, 2002; Li et al., 2003; Hasheminejad and Azarpeyvand, 2003, 2004; Ye et al., 2012; Li et al., 2014; Guo et al., 2017; Zhao et al., 2020; Marsick et al., 2021) and in a fluid with complex acoustic boundaries such as two surface meeting in a corner to create a quarter-infinite fluid domain (Chen et al., 2016; Guo et al., 2018). However, there is no analytical model for vibroacoustic analysis of an immersed cylindrical shell in water bounded by an upper free surface and lower rigid surface (i.e., shallow water). Therefore, for the first time, this work analytically formulates the forced vibroacoustic response of an infinite cylindrical shell in an underwater acoustic waveguide.

Partially submerged cylindrical shells were investigated in half-space domains where the shell is said to have a dry part that is exposed above the free surface of a fluid, and a wet part that is submerged in a fluid such as water. For example, Salaün (1991) provided an analytical approach in a wavenumber domain for evaluating the far field sound pressure for configurations of an open and closed infinite cylindrical shell under point force excitation. The shells are

*Corresponding author
jamie.kha@student.uts.edu.au (J. Kha)
ORCID(s):

partially submerged in a half-space of fluid. It is highlighted that the far field pressure is not always lowered when the excitation is positioned on the dry part of the shell, and that the effect of the free surface significantly affects the acoustic response of the partially submerged shell when compared to that of a shell in an infinite fluid domain. Li et al. (2003) extended this investigation by considering an infinite cylindrical shell with internal fluid, applying the same wavenumber domain approach as in Salaün's study. Parametric studies on the structural damping and thickness of the shell are included and found to be important in the far field sound pressure. Ye et al. (2012) investigated the different immersion depths of the submerged shell under point force excitation. The study notices that the far field pressure is significantly affected by the differing immersion status, while the input power flow is much less affected. Recently, Zhao et al. (2020) has presented theoretical investigations of a partially submerged shell of finite length, using a discretization approach of the wet surface to solve the vibroacoustic coupling of the shell and fluid domain. The vibration and acoustic results were related against immersion configurations from a completely wet shell to a completely dry shell using a frequency-depth spectra. Fringes from the interference of radiated acoustic waves were predicted in the spectra and validated against experimental results.

Completely submerged shells with a free surface or rigid surface are more relevant for the study of underwater structures, as partially submerged shells are more akin to studies of ships, and can provide benchmark comparisons to the extreme cases of a waveguide solution (i.e., where one of the acoustic boundary becomes significantly far from the shell). Ergin and Temarel (2002) investigated the wet dynamic characteristic of a submerged infinite cylindrical shell using the boundary integral equation and image source method to impose the free surface condition. The shell was filled at different capacities and compared against experimental measurements, demonstrating the method provides good results. Hasheminejad and Azarpeyvand (2003, 2004) provided acoustic analysis of an infinite cylindrical shell with a certain surface velocity distribution and near a boundary of a half-space of fluid, bounded by a rigid surface or impedance plane. These investigations did not involve cylindrical shells under excitation loads, rather applied a prescribed surface velocity distribution. Li et al. (2014) investigated an infinite cylindrical shell under point force excitation and near a free surface of a heavy fluid. The fluid-structure coupling is enforced by the image source method to account for the free surface, and Graf's addition theorem to reconcile the different coordinate system of the image source. An analytical expression for the far field sound radiation is then derived by applying the stationary phase approximation. Results of the far field characteristics demonstrate that there is significant influence of the depth of the free surface, and oscillations are observed with variation of the depth of the free surface and frequency. The work by Li et al. (2014) was extended by Guo et al. (2017) in which the far field sound is investigated for a finite cylindrical shell instead. In their work, vibration of the shell is initially solved analytically and used as an input to a BEM model to determine the far field sound pressure. It is observed in the study that there is a certain value of the submerged depth in which the vibration of the shell tends to be the same as the infinite fluid case. These studies have presented far field pressure investigations, which neglect the important near-field phenomena. Recently, Marsick et al. (2021) presented a complete vibroacoustic model in which the analytical expression for the pressure is presented for an infinite cylindrical shell near a free surface and under line-distributed load. This simplifies the model due to longitudinal symmetry, to a system akin to a two-dimensional thin ring under point force excitation. The near-field and far-field characteristics of the shell can be evaluated with this analytical approach.

More complex acoustic boundaries have also been investigated in literature, which involve a quarter-infinite domain of fluid. This refers to two boundary surfaces meeting at a corner to create a quarter-infinite domain. It is commonly referred as the double reflection scenario, and was investigated by a study by Chen et al. (2016). In their study, a free surface and a rigid surface meet at a corner and the free vibration of an infinite cylindrical shell is presented. The proposed method implements the image source method to develop the double reflection scenario, and the results are shown to be good compared against an FEM solution. Guo et al. (2018) extended the work by Chen et al. (2016), where an infinite cylindrical shell is under line-distributed load. From the investigation, it is emphasized that complex acoustic boundaries cannot be ignored as the directivity and far field sound pressure significantly vary with the distance between the shell and the boundaries.

The most applicable model to a shallow water is a waveguide formed by typically an upper free surface and lower rigid floor. However, there are few investigations and no analytical vibroacoustic model that completely describes the infinite cylindrical shell in an underwater waveguide. A general investigation of floating bodies in shallow water can be found by Jiang et al. (2018), where an integrated calculation method for the acoustic radiation and propagation has been developed with consideration of the sound velocity profile of the ocean environment. The associated Green's function for the fluid domain are derived using the image source method for the near-field and normal mode method for far-field, and examples of a sphere and elastic capsule in shallow water are presented. The results are compared against an FEM

simulation, and the method is shown to be computationally efficient. Similarly, Qian et al. (2021) provide a general method using a hybrid approach that involves wave-superposition method and multi-physical-coupled FEM. Examples of a pulsating sphere and elastic spherical shell in shallow water are demonstrated. These general studies provide an overview on the shallow water problem, without consideration of vibration from the structures. For a submerged shells in shallow water, the vibration of the structure can be specified by the equations of motion. The shell in shallow water was investigated by Wang et al. (2017), where a free vibration analysis is performed for a finite cylindrical shell in shallow water with different end supports. The analytical approach presents an approximation to the fluid-structure coupling by emphasizing the dominance of the real source contribution over the infinite image sources. Zhang et al. (2020) provides an FEM/BEM analysis of a slender shell in uniform shallow sea. The study identified that the seabed is most influential in the far field acoustic radiation of the shell. Aside from these studies, there are no other studies in literature that investigate the vibroacoustics of submerged shells in shallow water, especially, with an analytical approach.

In this paper, an analytical vibroacoustic model for an infinite cylindrical shell under line-distributed harmonic excitation is presented. The shell is submerged in an underwater waveguide formed by an upper free surface, that is modelled with a pressure release condition, and a lower rigid floor (seabed). The analytical approach involves solving the equations of motion of a thin shell based on Flügge's theory, and using image source method with Graf's addition theorem to implement the infinite reflections from the waveguide system. Longitudinal symmetry is applied to simplify the model to a single two-dimensional plane orthogonal to the longitudinal axis. The vibroacoustic response from the proposed analytical model is verified by numerical results obtained from an FEM model in COMSOL. Investigations of the effect of the standing waves criterion due to the waveguide on the acoustic response, importance of the contribution of image sources to the vibroacoustic response by comparison against the so-called "mirror effect" model, a comparison of acoustic wave propagation through the waveguide with two force configurations with a pulsating monopole source, and limiting cases of the waveguide configurations are presented.

## 2. Model

An infinitely long cylindrical shell of thickness $h$, mean radius $R$, Young's modulus $E$, Poisson's ratio $\mu$, and density $\rho_s$ is completely submerged in a heavy fluid of density $\rho_f$ and sound of speed $c_f$, as shown in Fig. 1. Structural damping loss factor $\eta$ is considered by a complex Young's modulus $E^* = E(1-\eta j)$ and fluid damping $\eta_f$ by considering a complex sound speed of the heavy fluid $c_f^* = c_f\left(1-\eta_f j\right)$. The fluid domain considered is a waveguide that is formed by the upper free surface and lower rigid floor, where the upper free surface is assumed to be a pressure release boundary condition. The total depth of the waveguide is $H > 2R$, where the distance from the origin (centre of the shell) to the upper free surface is $H_{\mathrm{fs}} > R$ and the origin to the rigid floor is $H_{\mathrm{sb}} > R$. The shell is excited by a harmonic line force $f_{\mathrm{e}}$ at the surface of the shell at an angle of $\varphi_0$ and along the $z$ direction. The system is described by cylindrical coordinates $(r, \varphi, z)$.

### 2.1. Motion of shell

Due to the line force excitation the system can be reduced to a two dimensional problem, where the motion of the shell is equivalent at any point along the $z$ direction. In this way, the radial displacement of the shell can be described by Flügge's shell equations of motion. Flügge's model is conventionally used to describe vibration of thin cylindrical shells (Li et al., 2014; Wang et al., 2017; Marsick et al., 2021). It provides an optimal trade-off between complexity of the phenomenon and relative simplicity of its mathematical treatment. For more information on Flügge's and other thin shell models, see Leissa (1993). A thin shell theory is used when the thickness is less than $1/20$ of the wavelength of deformation mode, allowing the shear deformation and rotary inertia to be neglected in dynamic analysis (Qatu, 2002). The equation is given as

$$\frac{1}{\gamma}\left(-\frac{\frac{d^2}{d\varphi^2}}{\frac{d^2}{d\varphi^2}+R^2\Omega^2}+K^2\frac{d^4}{d\varphi^4}+2\frac{d^2}{d\varphi^2}+1+K^2-R^2\Omega^2\right)w(\varphi)=f_{\mathrm{e}}-f_{\mathrm{p}}, \tag{1}$$

where $w$ is the radial displacements of the cylindrical shell, $f_{\mathrm{e}}$ is a line force excitation, $f_{\mathrm{p}}$ is heavy fluid loading, $\gamma = R^2\left(1-\mu^2\right)/(E^*h)$, $K = h^2/\left(12R^2\right)$, $\omega$ is angular frequency and $\Omega = \omega\sqrt{\rho_s R^2\left(1-\mu^2\right)/E}$ is frequency

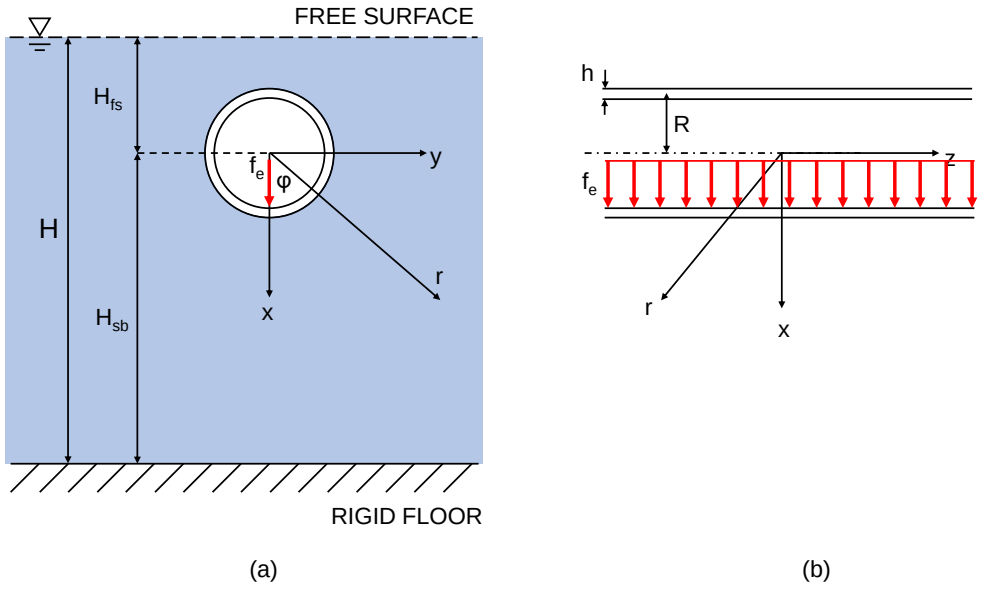


**Figure 1:** Schematic of the (a) front view and (b) side view for an infinitely long cylindrical shell completely submerged in a waveguide excited by a line-distributed force.

non-dimensionalized by the ring frequency of the cylindrical shell. The Fourier series of the subsequent spatial-dependent coefficients, the radial displacement of the shell and fluid loading pressure term are assumed to be expanded as such (Junger and Feit, 1986)

$$w(\varphi) = \sum_{n=-\infty}^{\infty} W_n \, e^{jn\varphi}, \tag{2}$$

$$p(r, \varphi) = \sum_{n=-\infty}^{\infty} P_n(r) \, e^{jn\varphi}, \tag{3}$$

$$f(\varphi) = \sum_{n=-\infty}^{\infty} F_n \, e^{jn\varphi}, \tag{4}$$

where $j = \sqrt{-1}$, and $W_n$, $P_n$ and $F_n$ represents the Fourier coefficients of the shell radial displacement, fluid loading pressure and force excitation respectively. From substituting Eqs. (2)-(4) into Eq. (1), and applying the Fourier transform, the spectral Flügge's equation of motion is given as

$$\frac{1}{\gamma}\left[-\frac{n^2}{n^2 - R^2\Omega^2} + 1 + K\left(n^4 - 2n^2 + 1\right) - R^2\Omega^2\right] W_n = F_{e,n} - F_{p,n}. \tag{5}$$

A line force excitation expressed by

$$f_e(\varphi) = \frac{F_0}{R}\delta\left(\varphi - \varphi_0\right), \tag{6}$$

where $F_0$ is the magnitude of the force and $\delta(\,)$ is the Dirac delta function. The Fourier transform of the excitation force is

$$F_{e,n} = \frac{F_0 e^{-jn\varphi_0}}{2\pi R}. \tag{7}$$

Solving for the coefficients of the radial displacement results in the following expression

$$W_n = \gamma T^{-1} \left( F_{\mathrm{e},n} - F_{\mathrm{p},n} \right), \tag{8}$$

where $T = -\frac{n^2}{n^2 - R^2\Omega^2} + 1 + K\left(n^4 - 2n^2 + 1\right) - R^2\Omega^2$. The remaining term to be determined is fluid loading $F_{\mathrm{p},n}$ which is related to the acoustic pressure.

## 2.2. Acoustic pressure in the underwater waveguide

In the acoustic domain, the radiated pressure from the vibrating shell satisfies the homogeneous Helmholtz equation

$$\nabla^2 p + k^2 p = 0, \tag{9}$$

where $k = \omega / c_f^*$ is the acoustic wavenumber and $p$ is the total pressure for a point in the acoustic field. For an infinite cylindrical shell in shallow water, there are four fluid domain boundary conditions that are imposed. The pressure release boundary condition of the upper free surface

$$p|_{\mathrm{fs}} = 0, \tag{10}$$

where the subscript $_{\mathrm{fs}}$ denotes points at the free surface, and the rigid floor condition of the lower seabed

$$\left.\frac{\partial p}{\partial n}\right|_{\mathrm{sb}} = 0, \tag{11}$$

where the subscript $_{\mathrm{sb}}$ denotes points at the seabed. Continuity at the surface of the shell to the external fluid is considered with Euler's relation

$$\frac{\partial p}{\partial r}(R, \varphi) = \omega^2 \rho_f \, w(\varphi). \tag{12}$$

These constraints imposed on the fluid domain result in reflections that contribute to the total acoustic pressure, and can be modelled with an image-source method as follows

$$p = p^{\mathrm{r}} + \sum_{i=1}^{\infty} \left\{ p^{\mathrm{u},i} + p^{\mathrm{l},i} \right\}, \tag{13}$$

where $p^{\mathrm{r}}$ is the pressure from the original (real) source without considering reflections, and $i$ denotes an index for counting the images, u refers to the upper images and l refers to the lower images. Finally, the Sommerfeld radiation condition of the unbounded remaining edges of the fluid domain is considered in the form of the acoustic pressure, which is determined by solving the Helmholtz equation in cylindrical coordinates using a separation of variables technique. It is known that acoustic pressure, where a harmonic time dependence of $e^{-\mathrm{j}\omega t}$ is omitted for brevity, takes on the form (Williams, 1999)

$$p^{\mathrm{r}}(r, \varphi) = \sum_{n=-\infty}^{\infty} P_n^{\mathrm{r}} H_n^{(1)}(kr) \, e^{\mathrm{j}n\varphi}, \tag{14}$$

where $n$ is the expansion coefficient, $H_n^{(1)}(\,)$ is the Hankel function of the first kind and $P_n^r$ are the unknown pressure coefficients for the real source. Similarly, pressure from the image sources also satisfy the Helmholtz equation and have the same form

$$p^{\mathrm{s},i}\left(r^{\mathrm{s},i}, \varphi^{\mathrm{s},i}\right) = \sum_{n=-\infty}^{\infty} P_n^{\mathrm{s},i} H_n^{(1)}\left(k r^{\mathrm{s},i}\right) e^{jn\varphi^{\mathrm{s},i}}, \tag{15}$$

where $\mathrm{s} = \mathrm{u} \vee \mathrm{l}$, and, $r^{\mathrm{s},i}$ and $\varphi^{\mathrm{s},i}$ are in the coordinate systems of the images, and $P_n^{\mathrm{s},i}$ are the unknown pressure coefficients for the image sources.

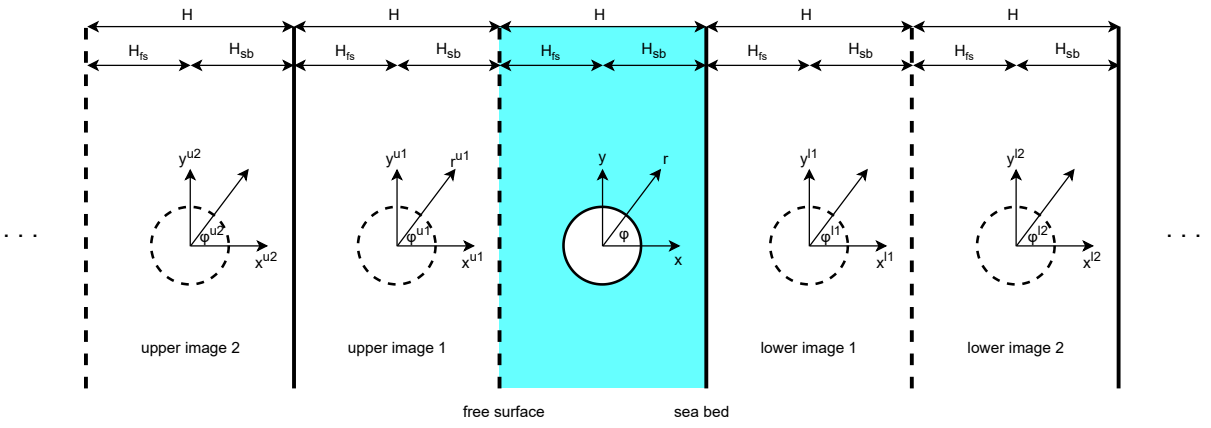


**Figure 2:** Images for an infinite cylindrical shell in an acoustic waveguide.

### *2.2.1. Free surface boundary condition*

We first aim to obtain an expression from the pressure release boundary condition of the free surface. Substituting Eqs. (13) - (15) into Eq. (10) gives

$$\sum_{n=-\infty}^{\infty} P_n^{\mathrm{r}} H_n^{(1)}\left(kr_{\mathrm{fs}}\right) e^{\mathrm{j}n\varphi} + \sum_{i=1}^{\infty}\sum_{n=-\infty}^{\infty}\left\{ P_n^{\mathrm{u},i} H_n^{(1)}\left(kr_{\mathrm{fs}}^{\mathrm{u},i}\right) e^{\mathrm{j}n\varphi^{\mathrm{u},i}} + P_n^{\mathrm{l},i} H_n^{(1)}\left(kr_{\mathrm{fs}}^{\mathrm{l},i}\right) e^{\mathrm{j}n\varphi^{\mathrm{l},i}}\right\} = 0, \tag{16}$$

where $r_{\mathrm{fs}}$ and $r_{\mathrm{fs}}^{i}$ are radial distances to the free surface from the real source and images, respectively. Now by considering Fig. 2, symmetry about the free surface for pairs of sources emerges. The above expression is re-written as

$$\begin{aligned}&\sum_{n=-\infty}^{\infty} P_n^{\mathrm{r}} H_n^{(1)}\left(kr_{\mathrm{fs}}\right) e^{\mathrm{j}n\varphi} + \sum_{n=-\infty}^{\infty} P_n^{\mathrm{u},1} H_n^{(1)}\left(kr_{\mathrm{fs}}^{\mathrm{u},1}\right) e^{\mathrm{j}n\varphi^{\mathrm{u},1}} + \\ &\sum_{i=1}^{\infty}\left\{\sum_{n=-\infty}^{\infty} P_n^{\mathrm{u},i+1} H_n^{(1)}\left(kr_{\mathrm{fs}}^{\mathrm{u},i+1}\right) e^{\mathrm{j}n\varphi^{u,i+1}} + \sum_{n=-\infty}^{\infty} P_n^{\mathrm{l},i} H_n^{(1)}\left(kr_{\mathrm{fs}}^{\mathrm{l},i}\right) e^{\mathrm{j}n\varphi^{\mathrm{l},i}}\right\} = 0,\end{aligned} \tag{17}$$

where $r_{\mathrm{fs}}$, $r_{\mathrm{fs}}^{\mathrm{u},i}$ and $r_{\mathrm{fs}}^{\mathrm{l},i}$ denote the radial distances to the free surface from the original source, $i$-th upper image and $i$-th lower image, respectively. From the symmetry of pair of sources about the free surface, it is noticed that $r_{\mathrm{fs}} = r_{\mathrm{fs}}^{\mathrm{u},1}$, $r_{\mathrm{fs}}^{\mathrm{u},i+1} = r_{\mathrm{fs}}^{\mathrm{l},i}$, and, for circumferential angles $\varphi + \varphi^{\mathrm{u},1} = \pi$ and $\varphi^{\mathrm{u},i+1} + \varphi^{\mathrm{l},i} = \pi$. These conditions are applied to the expression, and, for every second summation term, the expansion coefficient is exchanged from $n$ to $-n$ such that the Hankel property function $H_n^{(1)}(\xi)/H_{-n}^{(1)}(\xi) = (-1)^n$ can be employed. Now, looking at an $n$-th terms, the following expansion is obtained

$$\left[P_n^{\mathrm{r}} + P_{-n}^{\mathrm{u},1}\right] H_n^{(1)}\left(kr_{\mathrm{fs}}\right) + \sum_{i=1}^{\infty}\left\{\left[P_n^{\mathrm{u},i+1} + P_{-n}^{\mathrm{l},i}\right] H_n^{(1)}\left(kr_{\mathrm{fs}}^{\mathrm{u},i+1}\right)\right\} = 0. \tag{18}$$

The only solution to the expression is when all the multipliers of the Hankel functions are simultaneously equal to zero i.e.

$$P_n^{\mathrm{r}} + P_{-n}^{\mathrm{u},1} = 0 \quad \wedge \quad P_n^{\mathrm{u},i+1} + P_{-n}^{\mathrm{l},i} = 0. \tag{19}$$

### 2.2.2. Rigid floor boundary condition

The other boundary condition to consider is the rigid floor of the seabed. Chain rule is employed to convert the condition of Eq. (11) into the same coordinates of the problem, which are in cylindrical coordinates

$$\left.\frac{\partial p}{\partial x}\right|_{\text{sb}} = \left.\left\{ \frac{\partial p}{\partial r}\frac{\partial r}{\partial x} + \frac{\partial p}{\partial \varphi}\frac{\partial \varphi}{\partial x} \right\}\right|_{\text{sb}} = 0. \tag{20}$$

It is noticed from relating the cartesian and cylindrical coordinate systems that $\partial r/\partial x = \cos(\varphi)$ and $\partial \varphi/\partial x = -\sin(\varphi)/r$. Substituting Eqs. (13) - (15) into Eq. (20) gives

$$\begin{aligned}
&\sum_{n=-\infty}^{\infty} P_n^{\text{r}} e^{\text{j}n\varphi} \left[ kH_n^{(1)'}(kr)\cos(\varphi) - \text{j}n\frac{H_n^{(1)}(kr)}{r}\sin(\varphi) \right] + \\
&\sum_{i=1}^{\infty}\sum_{n=-\infty}^{\infty} \left\{ P_n^{\text{u},i} e^{jn\varphi^{\text{u},i}} \left[ kH_n^{(1)'}\left(kr^{\text{u},i}\right)\cos\left(\varphi^{\text{u},i}\right) - \text{j}n\frac{H_n^{(1)}\left(kr^{\text{u},i}\right)}{r^{\text{u},i}}\sin\left(\varphi^{\text{u},i}\right) \right] + \right. \\
&\left. P_n^{\text{l},i} e^{\text{j}n\varphi^{\text{l},i}} \left[ kH_n^{(1)'}\left(kr^{\text{l},i}\right)\cos\left(\varphi^{\text{l},i}\right) - \text{j}n\frac{H_n^{(1)}\left(kr^{\text{l},i}\right)}{r^{\text{l},i}}\sin\left(\varphi^{\text{l},i}\right) \right] \right\} = 0.
\end{aligned} \tag{21}$$

Similarly to the free surface condition, there is a symmetry about the lower rigid floor for pairs of sources. It is noticed that $r_{\text{sb}} = r_{\text{sb}}^{\text{l},1}$, $r_{\text{sb}}^{\text{l},i+1} = r_{\text{sb}}^{\text{u},i}$, and, for circumferential angles $\varphi + \varphi^{\text{l},1} = \pi$ and $\varphi^{\text{l},i+1} + \varphi^{\text{u}} = \pi$. Following a similar procedure as outlined in Section 2.2.1, the following relations emerges

$$P_n^{\text{r}} - P_{-n}^{\text{l},1} = 0 \quad \wedge \quad P_n^{\text{l},i+1} - P_{-n}^{\text{u}} = 0. \tag{22}$$

Combining the relations in Eqs. (19) and (22) completely relates each and every image coefficient to the original source coefficient. However, it is realized that every other image coefficient ($i = 2, 4, 6, \dots$) will be related to $P_{-n}^{\text{r}}$ instead of $P_n^{\text{r}}$. The image source coefficients is then related to the original source coefficient as

$$P_{-n}^{\text{u},I} = \begin{cases} -P_n^{\text{r}} & \text{if } I = 4i-3, \\ -P_{-n}^{\text{r}} & \text{if } I = 4i-2, \\ P_n^{\text{r}} & \text{if } I = 4i-1, \\ P_{-n}^{\text{r}} & \text{if } I = 4i, \end{cases} \tag{23}$$

and

$$P_{-n}^{\text{l},I} = \begin{cases} P_n^{\text{r}} & \text{if } I = 4i-3, \\ -P_{-n}^{\text{r}} & \text{if } I = 4i-2, \\ -P_n^{\text{r}} & \text{if } I = 4i-1, \\ P_{-n}^{\text{r}} & \text{if } I = 4i. \end{cases}$$

### 2.2.3. Kinematic boundary condition (vibroacoustic interaction)

The last condition to consider is the interaction between the structure and acoustic domain (i.e., the vibroacoustic interaction), such that the fluid loading on the shell can be determined. Fluid loading is a force which can be deduced from the derivative of the acoustic pressure at the surface of the shell in the radial direction. As the acoustic pressure expression is defined by the coordinate systems of the original source and image sources, to obtain the derivative in the radial direction, it is necessary to express the acoustic pressure in the coordinate system of the original source. This is achieved by employing Graf's addition theorem.

According to the Graf's addition theorem for Bessel functions, for upper images, the polar coordinates of the origin of the real source coordinate system with respect to the origin of the upper image source coordinate systems are $\left(L_{\text{u}}, 0\right)$ where $L_{\text{u}}$ is the distance from the real source to an upper image source. The transformation will be (Lee and Chen,

2010)

$$H_{-n}^{(1)}\left(kr^{\mathrm{u},i}\right)e^{-\mathrm{j}n\varphi^{\mathrm{u},i}}=\begin{cases}\displaystyle\sum_{m=-\infty}^{\infty}(-1)^{m+n}\,H_{m+n}^{(1)}\left(kL_{\mathrm{u},i}\right)J_m\left(kr\right)e^{\mathrm{j}m\varphi}, r<L_{\mathrm{u},i},\\ \displaystyle\sum_{m=-\infty}^{\infty}(-1)^{m+n}\,J_{m+n}\left(kL_{\mathrm{u},i}\right)H_m^{(1)}\left(kr\right)e^{\mathrm{j}m\varphi}, r>L_{\mathrm{u},i},\end{cases}\tag{24}$$

while for lower images, the polar coordinates of the origin of the real source coordinate system with respect to the origin of the lower image source coordinate systems are $(L_{\mathrm{l},i},\pi)$, where $L_{\mathrm{l},i}$ is the distance from the real source to a lower image source. Therefore, the transformation is (Lee and Chen, 2010)

$$H_{-n}^{(1)}\left(kr^{\mathrm{l},i}\right)e^{-\mathrm{j}n\varphi^{\mathrm{l},i}}=\begin{cases}\displaystyle\sum_{m=-\infty}^{\infty}H_{m+n}^{(1)}\left(kL_{\mathrm{l},i}\right)J_m\left(kr\right)e^{\mathrm{j}m\varphi}, r<L_{\mathrm{l},i},\\ \displaystyle\sum_{m=-\infty}^{\infty}J_{m+n}\left(kL_{\mathrm{l},i}\right)H_m^{(1)}\left(kr\right)e^{\mathrm{j}m\varphi}, r>L_{\mathrm{l},i},\end{cases}\tag{25}$$

where $J_m(\,)$ is the Bessel function of the first kind of order $m$, and, $L_{\mathrm{u},i}$ and $L_{\mathrm{l},i}$ are the distances between the origin of the upper and lower image source to the origin of the original source, respectively. To apply this specific application of Graf's addition theorem for fluid loading $r<L_{\mathrm{u},i}$ and $r<L_{\mathrm{l},i}$, the expansion coefficients of the image terms are first exchanged from $n$ to $-n$ without loss of generality, to obtain the following expression for the total acoustic pressure from Eq. (13)

$$\begin{aligned}p\left(r,\varphi\right)=&\sum_{n=-\infty}^{\infty}P_n^{\mathrm{r}}H_n^{(1)}\left(kr\right)e^{\mathrm{j}n\varphi}+\\ &\sum_{i=1}^{\infty}\sum_{n=-\infty}^{\infty}\sum_{m=-\infty}^{\infty}\left\{P_{-n}^{\mathrm{u},i}\left(-1\right)^{m+n}H_{m+n}^{(1)}\left(kL_{\mathrm{u},i}\right)J_m\left(kr\right)e^{jm\varphi}+P_{-n}^{\mathrm{l},i}H_{m+n}^{(1)}\left(kL_{\mathrm{l},i}\right)J_m\left(kr\right)e^{\mathrm{j}m\varphi}\right\}.\end{aligned}\tag{26}$$

The expansion coefficients of the image sources are again exchanged, though now between $n$ and $m$ to give

$$\begin{aligned}p\left(r,\varphi\right)=&\sum_{n=-\infty}^{\infty}P_n^{\mathrm{r}}H_n^{(1)}\left(kr\right)e^{\mathrm{j}n\varphi}+\\ &\sum_{i=1}^{\infty}\sum_{n=-\infty}^{\infty}\sum_{m=-\infty}^{\infty}\left\{P_{-m}^{\mathrm{u},i}\left(-1\right)^{m+n}H_{m+n}^{(1)}\left(kL_{\mathrm{u},i}\right)J_n\left(kr\right)e^{\mathrm{j}n\varphi}+P_{-m}^{\mathrm{l},i}H_{m+n}^{(1)}\left(kL_{\mathrm{l},i}\right)J_n\left(kr\right)e^{\mathrm{j}n\varphi}\right\}.\end{aligned}\tag{27}$$

Pressure resulting from the heavy fluid loading on the shell surface (i.e., $r=R$) is then converted into a harmonic load term in Fourier space

$$F_{p,n}=P_n^{\mathrm{r}}H_n^{(1)}\left(kR\right)+\sum_{i=1}^{\infty}\sum_{m=-\infty}^{\infty}\left\{P_{-m}^{\mathrm{u},i}\left(-1\right)^{m+n}H_{m+n}^{(1)}\left(kL_{\mathrm{u},i}\right)J_n\left(kR\right)+P_{-m}^{\mathrm{l},i}H_{m+n}^{(1)}\left(kL_{\mathrm{l},i}\right)J_n\left(kR\right)\right\}.\tag{28}$$

Introducing Eq. (2) and Eq. (28) into Euler's relation from Eq. (12) provides the expression of the displacement coefficients as a function of the pressure coefficients

$$W_n=\frac{k}{\rho_f\omega^2}\left[P_n^{\mathrm{r}}H_n^{(1)'}\left(kR\right)+\sum_{i=1}^{\infty}\sum_{m=-\infty}^{\infty}\left\{P_{-m}^{\mathrm{u},i}\left(-1\right)^{m+n}H_{m+n}^{(1)}\left(kL_{\mathrm{u},i}\right)J_n'\left(kR\right)+P_{-m}^{\mathrm{l},i}H_{m+n}^{(1)}\left(kL_{\mathrm{l},i}\right)J_n'\left(kR\right)\right\}\right],\tag{29}$$

where $H_n^{(1)'}(\,)$ and $J_n'(\,)$ are the first derivative with respect to $kR$. Finally, by introducing the last two equations to the equation of motion of the shell in Eq. (8), linear equations are obtained where the pressure coefficients are the unknown terms

$$Z_n^{\mathrm{r}}P_n^{\mathrm{r}}+\sum_{i=1}^{\infty}\sum_{m=-\infty}^{\infty}\left\{Z_{mn}^{\mathrm{u},i}P_{-m}^{\mathrm{u},i}+Z_{mn}^{\mathrm{l},i}P_{-m}^{\mathrm{l},i}\right\}=F_{\mathrm{e},n},\ \text{for } n\in\mathcal{Z},\tag{30}$$

**Table 1**
Dimensions and material properties of the shell and fluid properties.

| Parameter | Value |
|---|---|
| Young's Modulus $E$ (GPa) | 210 |
| Poisson's ratio $\nu$ | 0.3 |
| Density of shell $\rho_s$ (kg m$^{-3}$) | 7850 |
| Density of fluid $\rho_f$ (kg m$^{-3}$) | 1000 |
| Speed of sound $c_f$ (m s$^{-1}$) | 1500 |
| Thickness of shell $h$ (mm) | 5 |
| Mean radius $R$ (mm) | 1002.5 |
| Structural damping $\eta$ | 0.01 |
| Fluid damping $\eta_f$ | 0.001 |

where

$$Z_n^{\mathrm{r}} = \frac{kT}{\gamma \rho_f \omega^2} H_n^{(1)'}(kR) + H_n^{(1)}(kR), \tag{31}$$

is the fluid loading impedance from the original source, and

$$Z_{mn}^{\mathrm{u},i} = (-1)^{m+n} H_{m+n}^{(1)}\left(kL_{\mathrm{u},i}\right) \left\{ \frac{kT}{\gamma \rho_f \omega^2} J_n'(kR) + J_n(kR) \right\}, \tag{32}$$

and

$$Z_{mn}^{\mathrm{l},i} = H_{m+n}^{(1)}\left(kL_{\mathrm{l},i}\right) \left\{ \frac{kT}{\gamma \rho_f \omega^2} J_n'(kR) + J_n(kR) \right\}, \tag{33}$$

are the contribution to the fluid loading impedances from the upper image sources and lower image sources, respectively. To solve for the pressure coefficients $P_n^{\mathrm{r}}$, the pressure coefficient relation in Eq. (23) is necessary. The pressure coefficients $P_n^{\mathrm{r}}$ are substituted back into Eq. (13), with the relation for pressure coefficients of the image sources from Eq. (23) and using the following relations

$$r^{\mathrm{s},i} = \begin{cases} \sqrt{\left[L^{\mathrm{u},i} + r\cos(\varphi)\right]^2 + \left[r\sin(\varphi)\right]^2} & \text{for upper images, s} = \mathrm{u}, \\ \sqrt{\left[L^{\mathrm{l},i} - r\cos(\varphi)\right]^2 + \left[r\sin(\varphi)\right]^2} & \text{for lower images, s} = \mathrm{l}, \end{cases} \tag{34}$$

$$\varphi^{\mathrm{s},i} = \begin{cases} \arctan\left[\dfrac{r\sin(\varphi)}{L^{\mathrm{u},i} + r\cos(\varphi)}\right] & \text{for upper images, s} = \mathrm{u}, \\ \pi - \arctan\left[\dfrac{r\sin(\varphi)}{L^{\mathrm{l},i} - r\cos(\varphi)}\right] & \text{for lower images, s} = \mathrm{l}, \end{cases} \tag{35}$$

the acoustic pressure at any point within the fluid domain can be evaluated. The pressure coefficients $P_n^{\mathrm{r}}$ can be substituted into Eq. (29) to calculate the Fourier coefficients from Eq. (2) that evaluate the radial shell displacement. Moreover, to evaluate the radial shell displacement, the displacement coefficients, $W_n$ of the Fourier decomposition from Eq. (2) can be estimated by substituting the values of the pressure coefficients into Eq. (29).

## 3. Numerical results

Numerical investigations using the developed analytical method is implemented with MATLAB. From herein, numerical results generated are for a thin cylindrical shell of the following specifications as summarized in Tab 1. From the analytical approach, there are several expressions in which the number of image sources are necessary

to be specified. To ensure the convergence of the results, the number of images are increased until the results are not changing. The number of images necessary for convergence of results is dependent on the frequency of interest. However, generally it does not exceed 1000 upper images and 1000 lower images. Specification of the number of circumferential modes of the shell is also necessary. To ensure that enough modes are satisfied at a specific excitation frequency of the shell, the following criterion for the cut-off circumferential order, $N_c$ is applied (Maxit and Ginoux, 2010)

$$N_c = \text{int}\left[M \cdot R\max\left(k_p, k\right)\right] + 1, \tag{36}$$

where $k_p$ is the equivalent fluid-loaded plate flexural wavenumber and $M$ is the margin coefficient ($M = 1.5$ is found to be sufficient).

### 3.1. Model verification

A corresponding 2-D finite element model that is shown in schematic Fig. 3 is created with the commercial software COMSOL Multiphysics (v5.6), and used to generate appropriate results for model verification of the analytical procedure. The model follows the same specifications of the shell and fluid as summarized in Tab. 1 with a point load of 1 N applied at the location of ($x = R$, $y = 0$). The pressure field is symmetric about the point load, and surrounding waveguide, which allows for a symmetry boundary condition to be applied and simplify the numerical computation to involve only half of the computational domain. To enforce the Sommerfeld radiation condition, a perfectly matched layer (PML) is applied on the boundary of the computational fluid domain which allows outgoing acoustic waves to dissipate into the far field with minimal reflections back towards the shell. In the frequency domain, the PML imposes a complex-valued coordinate transformation to the selected domain that makes the PML absorbing at a maintained wave impedance, and thus eliminating reflections at the interface. The PML is relatively large to accommodate for the large wavelengths exhibited by outgoing waves from the vibrating shell at low frequencies in water. The computational domain is discretized with a fine mesh to ensure accurate numerical predictions. This included ensuring at least ten elements per wavelength considered in the fluid domain. The fluid domain was modeled using the COMSOL Pressure Acoustics module, and the shell was modeled as a linear elastic medium using the Solid Mechanics module. To couple the pressure acoustics model with the structural component, the Acoustic-Structure boundary condition was applied. Numerical computations were then performed in a specified frequency range to determine the forced vibroacoustic response of the fully coupled fluid-shell system. The proposed analytical model is verified by comparing a variety of generated vibroacoustic results with those from an FEM simulation using COMSOL. A case study for the shallow waveguide is specified as $H = 4$ m, $H_{fs} = H_{sb} = 2$ m (i.e., a shell that is positioned at the midpoint of a waveguide with total depth of 4 m).

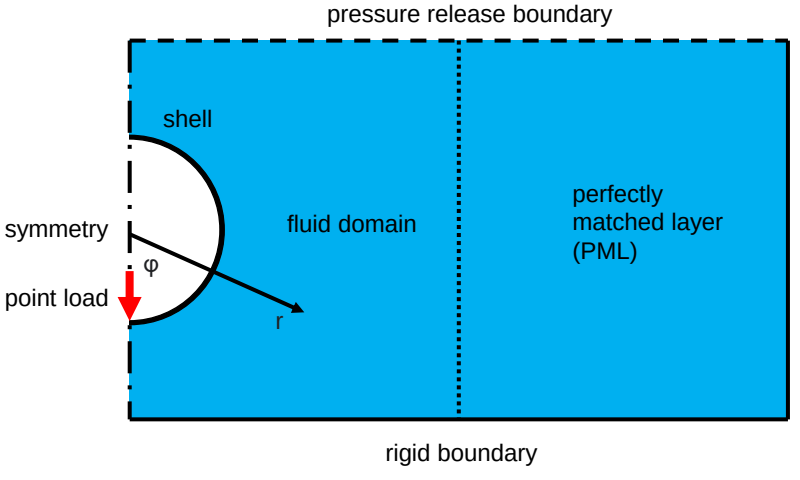


**Figure 3:** Schematic of the finite element model.

The structural response of the shell is first investigated by evaluating the spatial average of shell velocity (Williams, 1999) as

$$\langle v \rangle^2 = \frac{1}{S} \int_S |\dot{w}|^2 \, dS = \omega^2 \sum_{n=-\infty}^{\infty} |W_n|^2 , \tag{37}$$

where $S$ is the surface area of the shell. The results are shown in Fig. 4 and compared against those from a corresponding COMSOL model. It is observed that there is an excellent agreement between the results for almost the entire frequency range. There is a slight frequency shift that becomes more apparent at higher frequencies ($>$ 2000 Hz) due to the limitations of the thin shell theory applied in the analytical model which ignores transverse shear deformation whereas the FEM model includes it. Acoustic pressure is calculated for a field point that has been chosen to be close to the shell at ($r = 2$ m, $\varphi = \pi/2$). Using the analytical expression from Eq. 13, the pressure spectra is evaluated and shown in Fig. 5. Results are generated from a corresponding COMSOL model, and indicate excellent agreement. To further investigate the acoustic pressure characteristics, the acoustic pressure is evaluated in a spatial domain of 4 m $\times$ 6 m in the x-y plane of the shell as shown in Fig 6. The pressure field surrounding the shell are shown in Fig. 6 (a,b) for a low frequency of 90 Hz, which corresponds to the peak at low frequency from Fig. 5. The map of the acoustic pressure is also shown for a higher frequency of 1800 Hz in Fig. 6 (c,d), which corresponds to the greatest SPL value in the spectra from Fig. 5. The pressure distributions in the low frequency and higher frequency are different. For a low frequency, the number of circumferential modes observed in the near-field behavior of the shell is significantly less than that of a higher frequency. Additionally, the surrounding pressure fields differ – where the low frequency has a seemingly uniform distribution along the y-direction, whereas the higher frequency presents much more variation. Upon comparison with a corresponding COMSOL model, the results are shown to be in excellent agreement – demonstrating that the analytical model can predict the pressure field in proximity to the surface of the shell and in the surrounding fluid domain.

Aside from the structural and acoustic response of the shell, the energy output from the system is investigated. Radiated sound power is calculated by the following expression (Williams, 1999)

$$\Pi(\omega) = \frac{1}{2} \int_S \text{Real} \left\{ p(R, \varphi) \cdot \overline{\dot{w}}(\varphi) \right\} \, dS, \tag{38}$$

where the superscript — denotes the complex conjugate, $p(R, \varphi)$ is the pressure at the surface of the shell evaluated by Eq. (13), and $\dot{w}(\varphi)$ is the radial shell velocity calculated by taking the first derivative with respect to time of the radial shell displacement $\dot{w}(\varphi) = -j\omega \, w(\varphi)$. Power per unit length is evaluated due to the longitudinal symmetry of the line force excited shell, reducing the surface integral to a line integral over the circumference of the shell. Radiated sound power is evaluated by substituting Eqs. (2) and (3) into Eq. (38) to obtain the following

$$\Pi(\omega) = \pi \omega R \sum_{n=-\infty}^{\infty} \text{Real} \left\{ -j P_n \overline{W}_n \right\} . \tag{39}$$

Acoustic power is calculated for a shallow waveguide in Fig. 7 and the comparison against the corresponding COMSOL model is in very good agreement, except at the very low frequency. This can be attributed to the fact that acoustic wavelengths are quite large at low frequencies in water. Therefore, the PML may not be able to properly perform as a perfect non-reflecting boundary condition. It should be noted that the analytical model is several orders of magnitude more computationally efficient than the COMSOL model for evaluating these results. Additionally, there is significantly less data storage necessary for the analytical computations than with finite element simulations.

### 3.2. Effect of the waveguide on the vibroacoustic response

In the previous section, the present model is verified against corresponding COMSOL models to demonstrate its capability in accurately predicting the vibroacoustic behavior of a shell in shallow water. In this section, the effect of the waveguide on the vibroacoustic response is presented. Firstly, it is acknowledged that the fluid domain, being an acoustic waveguide, induces reflections that manifest as image source contributions to the vibroacoustic behavior. This will result in standing waves forming between the upper and lower acoustic boundaries of the waveguide, which is characterized by a standing waves criterion. In the present method, the vibroacoustic response is fully coupled, however, it is shown that there is a distinction between the present study and the so-called "mirror effect" model. The "mirror effect" model is an approximation in which the fluid-structure coupling ignores the influence of the image

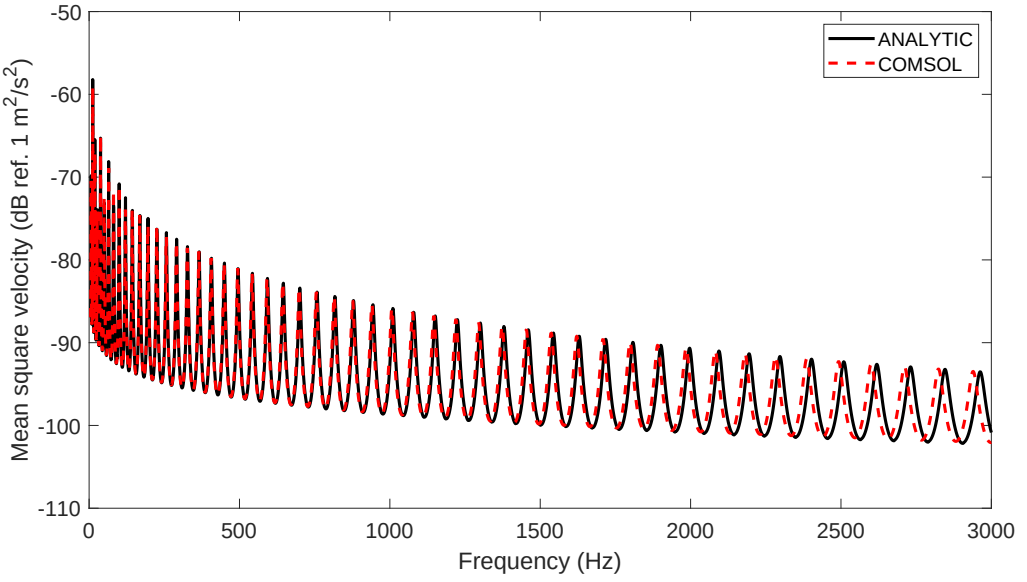


**Figure 4:** Spatial average of shell velocity for a waveguide $H = 4$ m, $H_{fs} = H_{sb} = 2$ m.

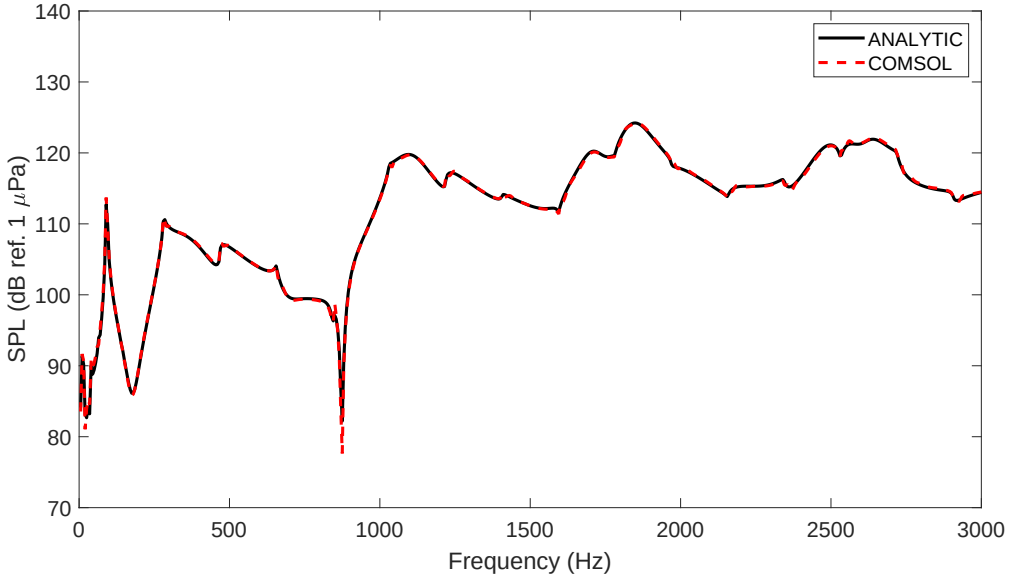


**Figure 5:** Acoustic pressure spectra at $(r = 2, \varphi = \pi/2)$ for a waveguide $H = 4$ m, $H_{fs} = H_{sb} = 2$ m.

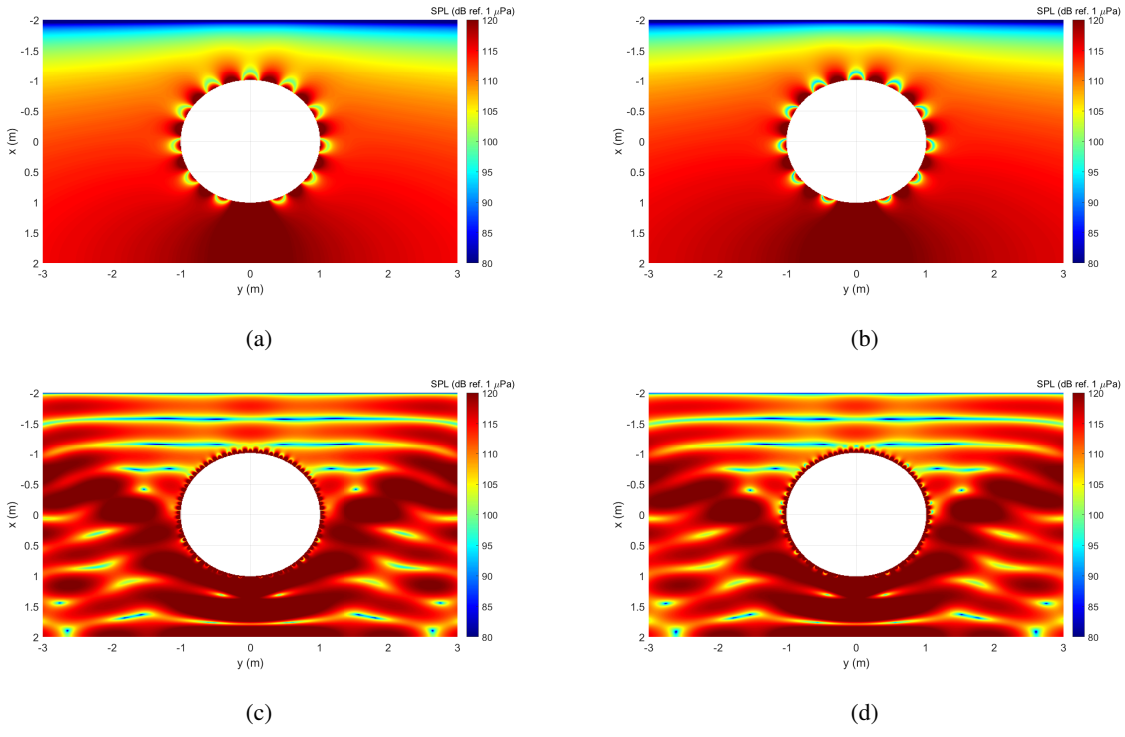


**Figure 6:** Pressure map of the (a) analytical result and (b) COMSOL result for a frequency of 90 Hz, and, the (c) analytical result and (d) COMSOL result for a frequency of 1800 Hz.

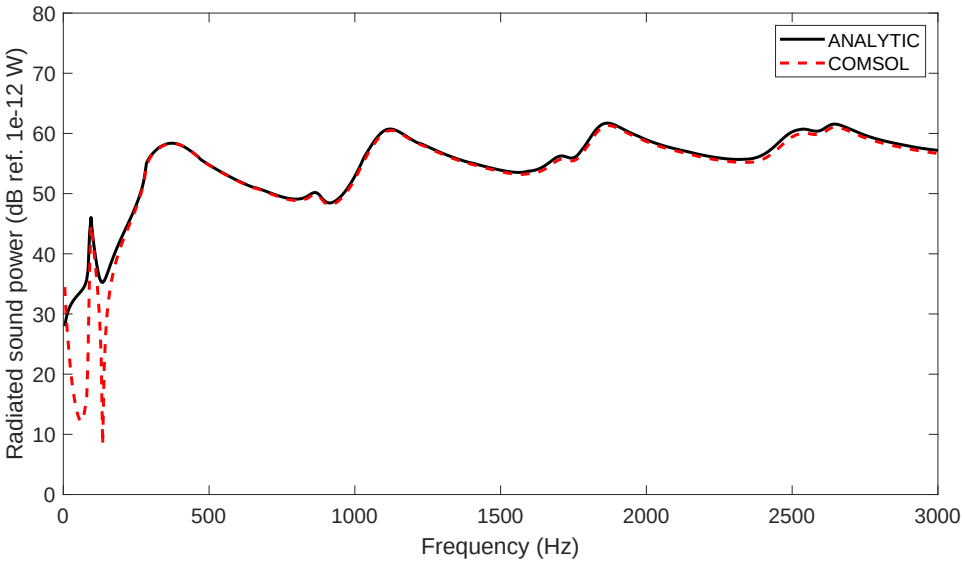


**Figure 7:** Acoustic power spectra for a waveguide $H = 4$ m, $H_{fs} = H_{sb} = 2$ m.

sources (i.e., reflections off the acoustic boundaries) in the fluid-structure coupling at the surface of the shell. The image source contributions are only implemented at the acoustic response of the shell. With this approximation there will be discrepancies in the contributions to the circumferential modes which are highlighted. Following this is an investigation into the acoustic propagation over a horizontal distance from the surface of the shell in the acoustic domain. The effect of the direction of point force loading and a comparison against a pulsating monopole is presented. Finally, there is an investigation into the limiting cases of waveguide configurations, in which the individual and combined effect of the acoustic boundaries can be deduced by comparison against results where the free surface is far enough away such that the waveguide is approximately a rigid floor only acoustic domain, the rigid floor is far enough away such that the waveguide is approximately a free surface only acoustic domain, and, both the free surface and rigid floor are far enough away such that the waveguide is approximately an unbounded fluid domain.

The following numerical results are presented using the formulation from Section 2, and the specifications are outlined in Tab. 1. It is noticed that the vibroacoustic behavior of a shell is not only sensitive to specifications of the fluid-shell system, but the waveguide dimensions and its position within it. As its interaction with an underwater waveguide is complex, the objective of this section is then to deliver general and intuitive results. It is noticed that results such as investigating the waveguide dimensions or relative position of the shell in the waveguide to the acoustic pressure spectra at a specific point is very much dependent on the direction of force excitation, making it difficult to draw upon any general conclusion from it.

### *3.2.1. Standing waves criterion*

Vibroacoustic behavior of structures within an acoustic waveguide can be coupled such that at certain frequencies, a standing wave can propagate within the space of the waveguide. In this case, an excited shell within an underwater waveguide can generate standing waves along the $x$-direction, perpendicular to the acoustic boundaries, at frequencies that are found by the standing waves criterion (Kha et al., 2022)

$$f_N^{\mathrm{sw}} = \frac{c_f}{4H}(2N+1), \quad N = 0, 1, 2, 3, \ldots . \tag{40}$$

These frequencies characterize the modes of the waveguide present in the system. The existence of these standing waves is first demonstrated in Fig. 8, where the pressure spectra for an excited shell in shallow water of total depth $H = 10$ m is presented. The standing waves criterion is observed for a point in the fluid domain that is far enough away from the shell, ($r = R + 10$ m, $\varphi = \pi/2$), that the structural modes in the near field of the shell does not interfere with the result. Additionally, in this figure, the transition between the resonance due to the structural modes of the shell to the resonance due to the standing waves criterion is observed. The pressure spectra is evaluated at three different observer points at increasing distances from the surface of shell: at the surface of the shell $r = R$, near the surface of the shell $r = R+1$ m, and far from the surface of the shell $r = R+10$ m. At the surface of the shell, the pressure spectra is dominated by the structural response of the shell, and the resonant peaks are due to the circumferential modes of the shell. It is worth noting that the $N = 1$ standing wave seems to have an influence on the pressure spectra at the surface of the shell, while the remaining standing wave frequencies do not. This can be explained as it is coincidentally occurring at the non-resonant area of the spectra. Other standing wave frequencies in this frequency range are in spectral proximity to a structural mode peak. At near the shell surface, $r = R + 1$ m, there is influence of the structural modes on the spectra at very low frequency, and the standing waves criterion is manifested at the remaining frequency range. When the observer point is chosen to be far enough away from the surface of the shell, $r = R + 10$ m, the pressure spectra is dominated by only the standing waves criterion, and information about the structural modes vanishes.

### *3.2.2. Mirror effect model*

The present method is considered a fully coupled approach in which the image sources due to the reflections off the acoustic boundaries of the waveguide are implemented in the fluid-structure coupling as well as the acoustic pressure. It is first recognized that the fully coupled method is distinguished from the so-called "mirror effect" model which is an approximation that considers the image sources from the waveguide in the total pressure in Eq. (13) and neglects the effects on the fluid-structure coupling, where in Eq. (30) the fluid loading impedances from the image sources ($Z_{mn}^{\mathrm{u},i}$ and $Z_{mn}^{\mathrm{l},i}$) are ignored. As a consequence, the pressure coefficients $P_n^{\mathrm{r}}$ evaluated from the differing approaches are not identical. This does not seem to have an effect on the vibrational response of the shell, as mentioned by Wang et al. (2017) in a free vibration study of an infinite cylindrical shell in a perfect underwater acoustic waveguide, though it does have significant differences in the acoustic response of the shell as shown by Marsick et al. (2021) in a study of

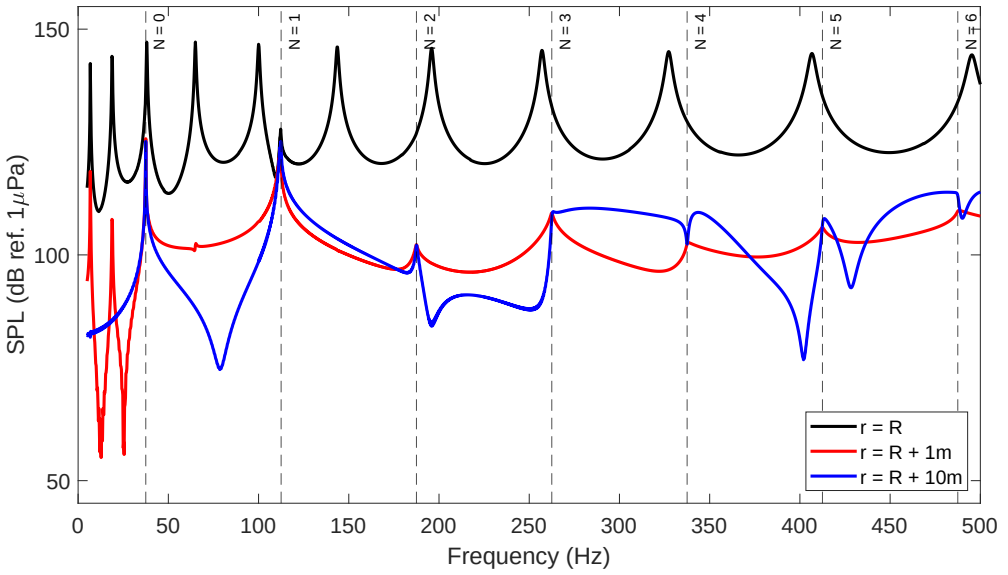


**Figure 8:** Acoustic pressure spectra for a vertically-loaded shell positioned at the midpoint of a waveguide of depth $H = 10$ m. The observation point is chosen at several locations including: at the surface of the shell ($r = R, \varphi = \pi/2$), 1m from the surface ($r = R + 1$ m, $\varphi = \pi/2$), and 10m from the surface ($r = R + 10$ m, $\varphi = \pi/2$).

forced acoustic response of an infinite cylindrical shell in a fluid domain with a free surface only. This is found to be the case as with the present study.

The following Figs. 9 and 10 presents a comparison between the fully coupled model and "mirror effect" model for an observer point chosen to be far enough away from the shell such that the influence of the near field effects are negligible. In Fig. 9, a shallow waveguide is chosen, and in this case the difference between the two models are important at the standing waves frequencies, as the amplitudes of the resonances are different. When the waveguide depth becomes larger, the discrepancy is less apparent as shown in Fig. 10. For an observer point at the surface of the shell, the pressure spectra (results not shown here) predicted by both models are seemingly identical. This difference in the vibroacoustic response in the fluid domain and similarity at the surface of the shell is explained in Fig. 11. In this figure, the first six non-negative circumferential modes of the shell are compared between the two models to highlight any differences. It is observed that for low circumferential modes ($n = 0, 1, 2, 3$), that there are significant differences in the predictions made between the two models. This discrepancy is not so important in its contribution to the structural response as the low mode orders are negligible. However, these discrepancies become significant for calculation of sound in the fluid domain as revealed in the discrepancies in the acoustic results presented in Figs. 9- 10. The peaks in these contributions correspond to the standing waves criterion, which further emphasize that the "mirror effect" model is not able to properly predict this phenomenon. However, at high enough circumferential modes ($n > 3$), those of which contribute to the structural response, it is observed that the prediction is identical between the two models. This explains why the predictions to the structural response is seemingly identical between the two model. Generally, it can be said that the structural response of the shell can be made by either model as the higher circumferential modes are well predicted. However, for acoustic results in the fluid domain, in which the low circumferential modes are important, the "mirror effect" model is not well adapted.

Pressure is now investigated along distance instead of frequency to further examine the "mirror effect". The results are shown in Fig. 12, where the acoustic propagation along the $y$-axis is presented for three frequencies, a low frequency that is not a standing wave frequency (100 Hz), an intermediary frequency that corresponds to $N = 3$ standing wave frequency (262.5 Hz), and a higher frequency that is also not a standing wave frequency (500 Hz). There is a deviation between the fully coupled model and mirror effect model at the low frequency, where there is a significant amplitude shift. At the standing wave frequency, in which the shell is very much coupled to the modes of the waveguide, there

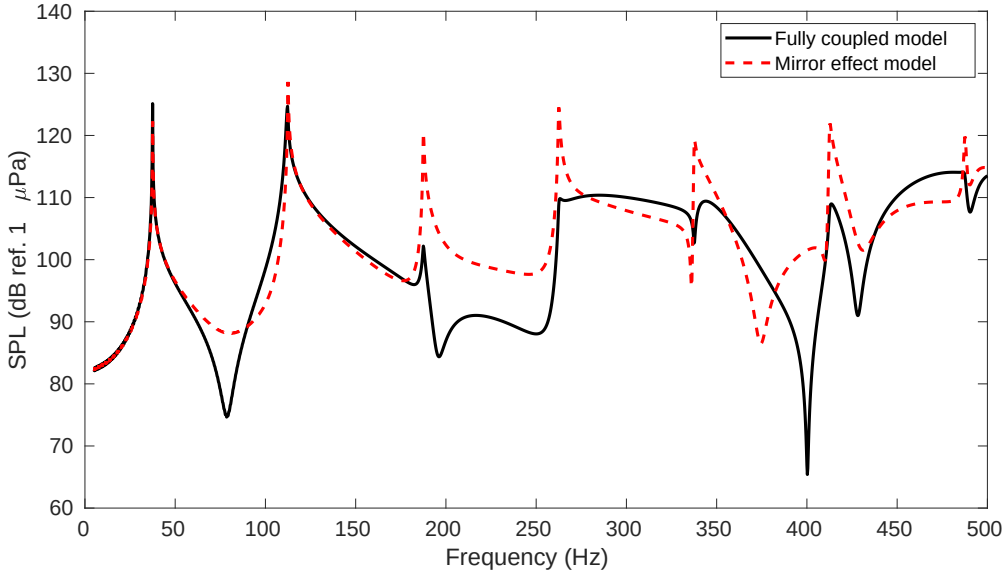


**Figure 9:** Acoustic spectra observed at $(r = R + 10 \text{ m}, \varphi = \pi/2)$ for a vertically-loaded shell positioned at the midpoint of a waveguide with total depth $H = 10$ m.

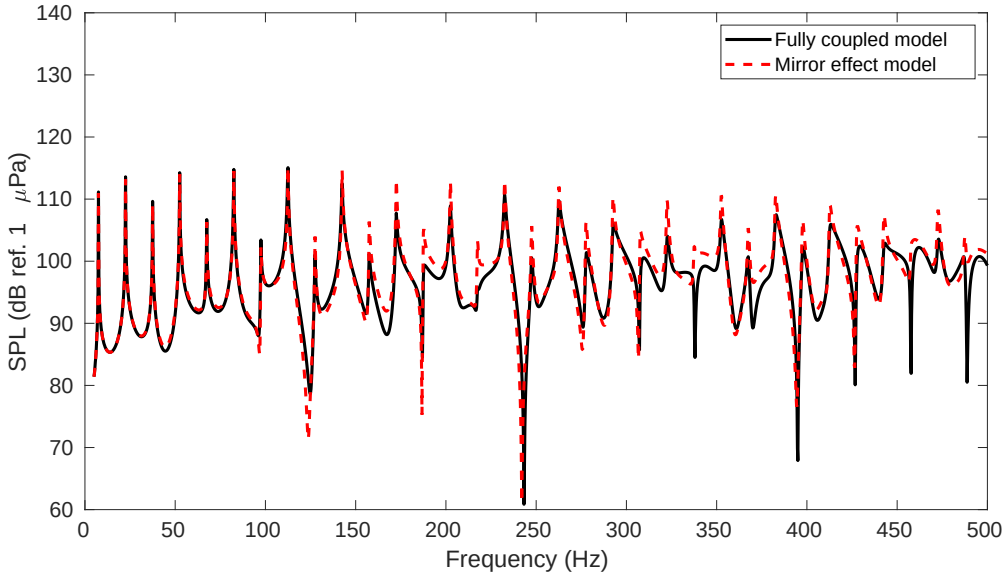


**Figure 10:** Acoustic spectra observed at $(r = R + 10 \text{ m}, \varphi = \pi/2)$ for a vertically-loaded shell positioned at the midpoint of a waveguide with total depth $H = 50$ m.

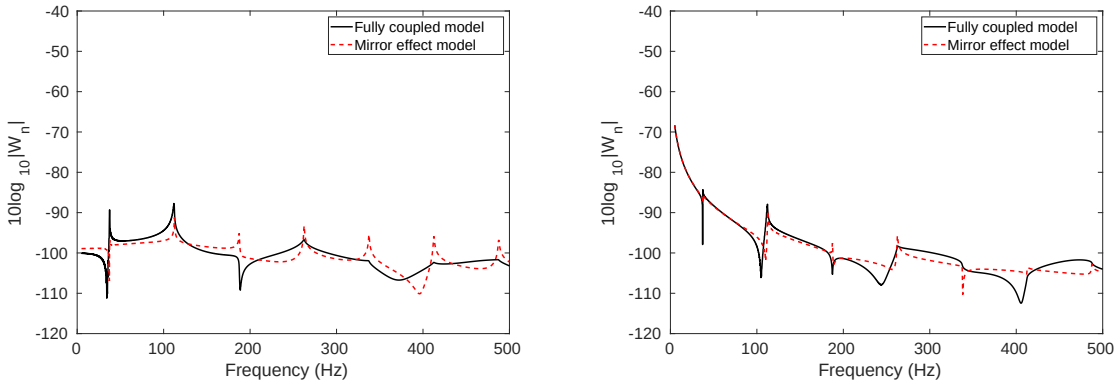


(a) $n = 0$ (b) $n = 1$

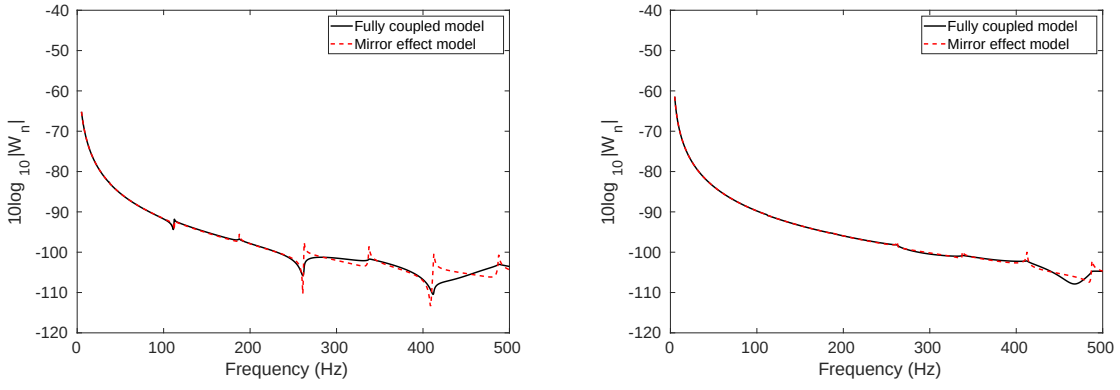


(c) $n = 2$ (d) $n = 3$

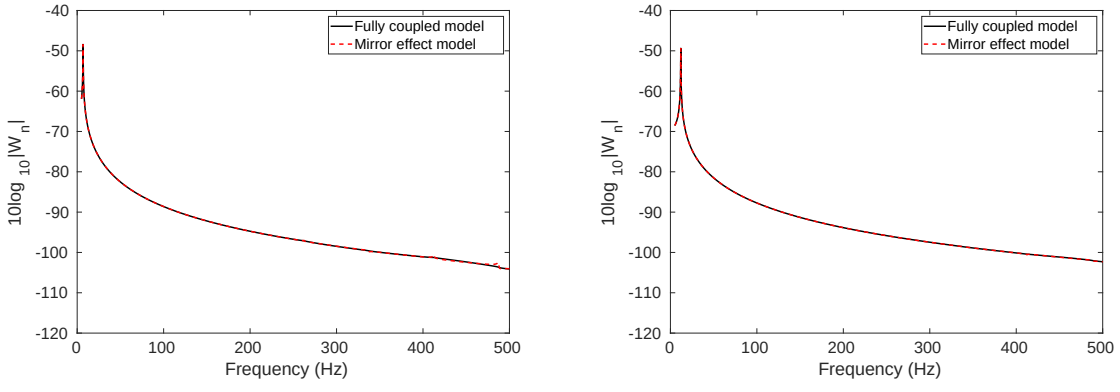


(e) $n = 5$ (f) $n = 6$

**Figure 11:** Contribution of the first six non-negative circumferential modes $(n = 0, 1, 2, 3, 4, 5)$ to the shell radial displacement.

is a substantial difference observed in the predictions. The oscillations are not similar, and this is found to occur at all the standing wave frequencies. At a higher frequency, shown here as 500 Hz, the difference is subtler, and becomes less apparent as the frequency increases even more. The fully coupled model fully satisfies all the boundary conditions. However, this is not the case for the mirror effect model where the effects of image sources (i.e., presence of the waveguide boundaries) are neglected from the fluid-structure coupling. This results in a discrepancy in the calculation of the low order modes and contributes to the accuracy of calculation of low frequency (low mode) acoustic propagation.

### *3.2.3. Comparison against a monopole*

The fully coupled model is used to investigate the influence of the direction of force applied to excite the shell on its acoustic propagation through the waveguide. Two force configurations are considered: a vertically loaded shell ($\varphi_0 = 0$), and a horizontally loaded shell ($\varphi_0 = \pi/2$). In the latter case, it is acknowledged that the force excitation is directly ahead of the observation points. The excited shell is then compared with a system in which a pulsating monopole replaces it at the origin of the shell. To describe the acoustic behavior of the pulsating monopole in a waveguide, the Green's function solution to the two-dimensional Helmholtz equation is required. For a pulsating monopole in a free field, the Green's function is the zero-th order Hankel function of the first kind (assuming $e^{-\mathrm{j}\omega t}$ time dependency) (Linton, 1998)

$$G\left(x, y, z; x_1, y_1, z_1\right) = -\frac{j}{4} H_0\left(kr\right). \tag{41}$$

The appropriate Green's function for a monopole in an ideal two-dimensional waveguide is then obtained by applying the image-source method, in which the Green's function for a monopole in free field for an infinite number of monopole image sources are added together. It will take the form of an infinite sum of zero-th order Hankel functions, that have simple coefficients due to the reflections off the acoustic boundaries.

The acoustic propagation results are shown in Fig. 13, where a comparison between a vertically loaded shell and horizontally loaded shell, and, between a horizontally loaded shell and pulsating monopole is presented. Three frequencies of interest are investigated, which include a low frequency that is not a standing wave frequency (100 Hz), an intermediary frequency that corresponds to $N = 3$ standing wave frequency (262.5 Hz), and a higher frequency that is also not a standing wave frequency (500 Hz). Upon observing these two comparisons, there are several qualitative remarks that can be made. At low frequencies, the vertically loaded shell exhibits oscillation, while for the horizontally loaded shell and pulsating monopole, below a certain frequency, it is relatively stable. At the standing wave frequencies, here shown for the $N = 3$ frequency, the vertically loaded shell and horizontally loaded shell share a similar shape, in that it is noticed the oscillations of the acoustic propagation is out of phase. While, for a horizontally loaded shell and a pulsating monopole, there is significant differences in the shape, though the oscillations remain in-phase. Generally, it is shown that the vertically loaded shell and horizontally loaded shell do not resemble each other in acoustic propagation. Whereas, a horizontally loaded shell and pulsating monopole have similar acoustic propagation, except at standing wave frequencies.

### *3.2.4. Limiting cases of the waveguide configurations*

Using the unbounded sea case as a reference, acoustic propagation is predicted for three different large waveguides: $H = 1000$ m, $H = 2000$ m and $H = 5000$ m in Fig. 14. The difference in the sound pressure level is evaluated such that $\Delta\mathrm{SPL} = 20\log_{10}\left|p/p_\infty\right|$, where $p_\infty$ is the acoustic pressure for a shell in an unbounded sea and is evaluated by having no images in the model, $p^{\mathrm{u},i} = p^{\mathrm{l},i} = 0$. If the difference in acoustic pressure is within the black dashed lines, it denotes convergence such that the difference is less than $\pm 1$ dB, and where convergence refers to which the waveguide becomes equivalent to the limiting case of an unbounded sea. From Fig. 14, the acoustic propagation along the $y$-axis is evaluated for the large waveguides at a low frequency (100 Hz), an intermediary frequency (300 Hz), and a higher frequency (500 Hz). It is observed that for a waveguide depth of $H = 5000$ m, it is sufficient for convergence even at low frequencies and it is generally observed that as the frequency is increased, the convergence of the sound propagation to the far field receivers occurs at smaller waveguide depths. For example, at 300 Hz, the waveguide depth of 2000 m is converged and at 500 Hz, the waveguide depth of 1000 m is nearing convergence. This is a consequence of the acoustic waves propagating at smaller wavelengths, and smaller in a relative sense to the waveguide depth. For a shallower waveguide, such as with depth of $H = 100$ m, the convergence will occur at very high frequencies, which is found to be approximately 5000 Hz (not shown here). It is then inferred that convergence is related to the frequency

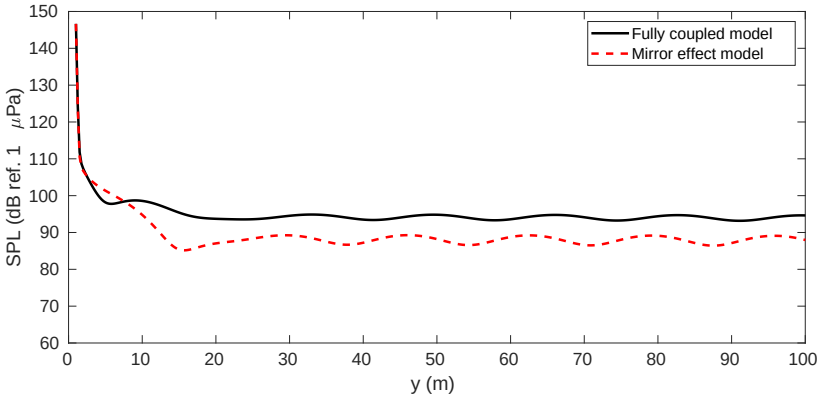


(a) 100 Hz (low frequency, non-standing wave frequency)

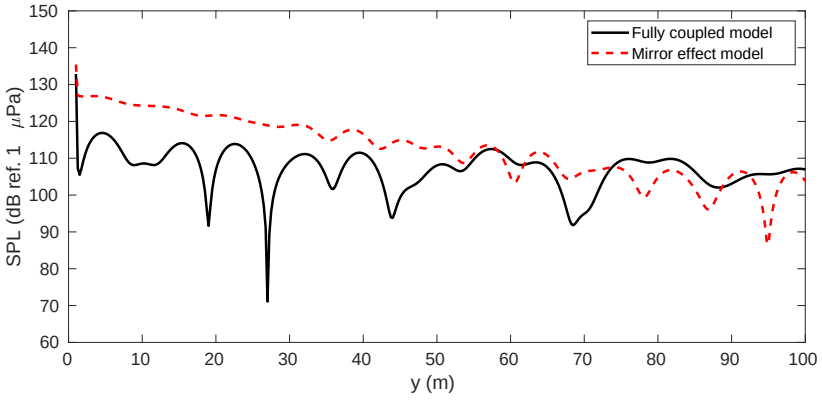


(b) 262.5 Hz ($N = 3$ standing wave frequency)

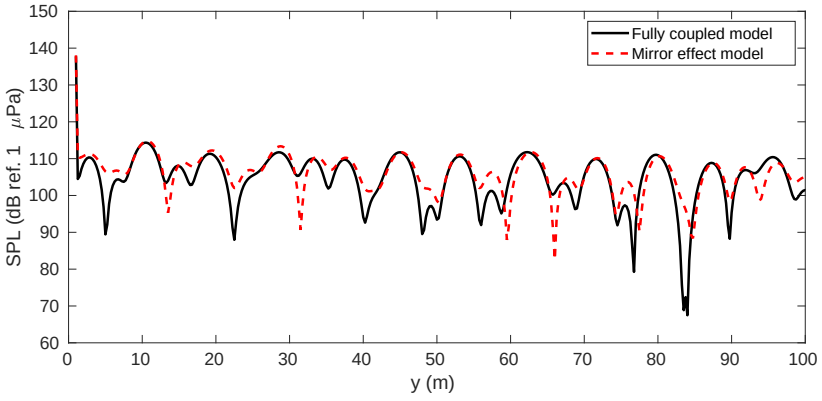


(c) 500 Hz (higher frequency, non-standing wave frequency)

**Figure 12:** Comparison of the fully coupled model (present study) and "mirror effect" model (approximation) for the acoustic sound pressure along $(x = 0, y)$ for a vertically-loaded shell positioned at the midpoint of a waveguide with total depth of $H = 10$ m.

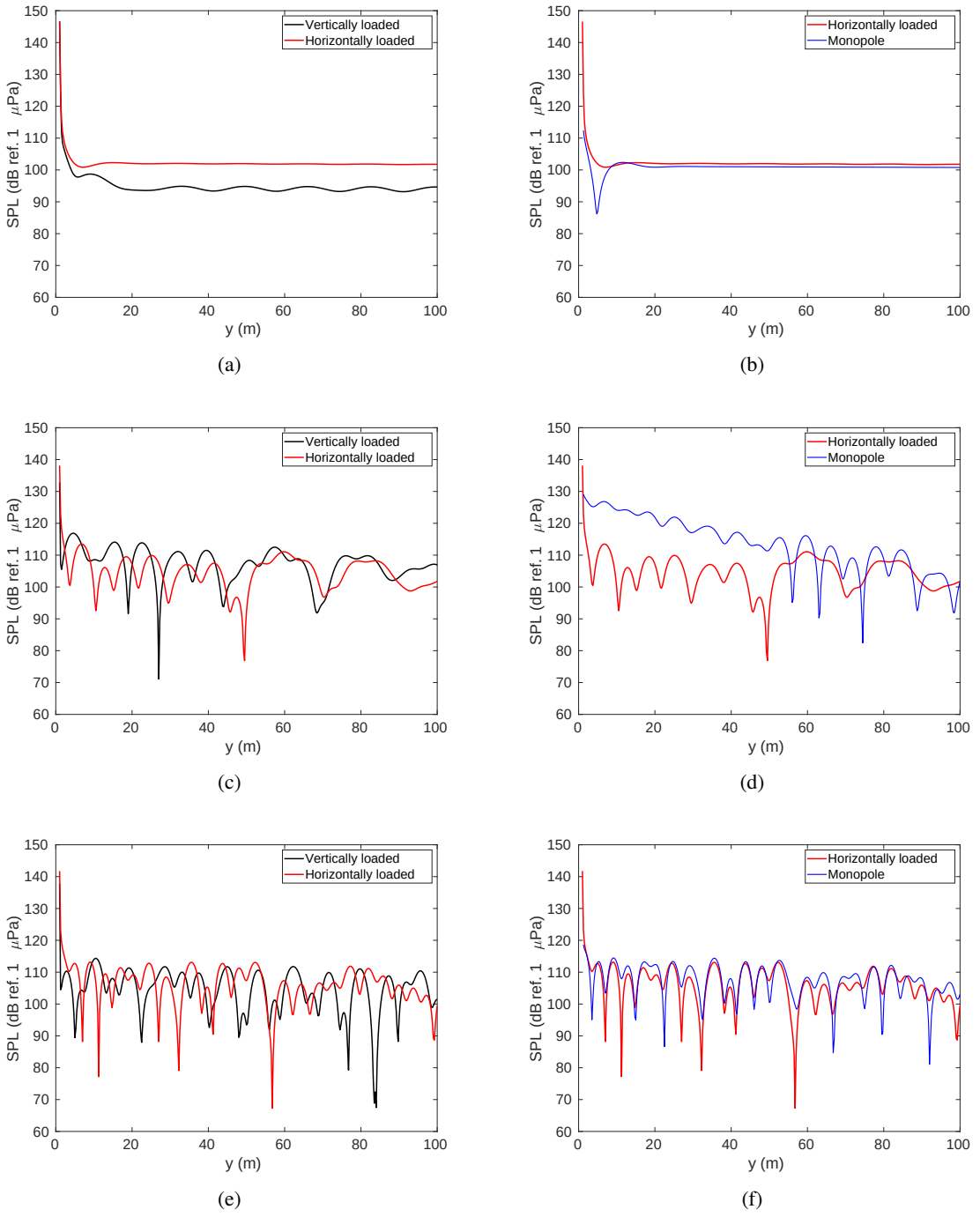


**Figure 13:** Acoustic sound pressure along $(x = 0, y)$ for a vertically loaded shell, horizontally loaded shell and pulsating monopole positioned at the midpoint of a shallow waveguide with total depth $H = 10$ m. Comparison between a vertically loaded shell and horizontally loaded shell (Left) and, between a horizontally loaded shell and pulsating monopole (Right) is shown for the following frequencies: 100 Hz (a,b), 262.5 Hz (c,d), and 500 Hz (e,f).

as a direct consequence to the relative size of the propagating waves become significantly smaller than the waveguide depths such that the waves are seemingly propagating in a free field. A good qualitative requirement is that the acoustic wavelengths are at least two orders of magnitude smaller than the waveguide depth.

Generally, it is understood that the vibroacoustic response of the shell is affected by its relative position in the waveguide and the waveguide dimensions. To limit the possibilities and present simple findings, the limiting cases of the waveguide configuration are investigated, starting with a shallow waveguide and comparing it against an unbounded fluid domain (i.e., both the free surface and rigid floor are far), a fluid domain with a free surface only (i.e., rigid floor is far) and a fluid domain with a rigid floor only (i.e., free surface is far) in Fig. 15. As a consequence of increasing the frequencies, the fluctuation of the acoustic pressure along the $y$ axis becomes increasingly unstructured as can be seen in Fig. 14. To simplify the observations in this investigation, a low frequency is chosen (150 Hz) such that the convergence to the limiting case would be no more than $H = 5000$ m, while maintaining some fluctuation along the $y$-axis for comparison. Two force configurations imposed on cylindrical shells are depicted in Fig. 15, a vertically loaded shell ($\varphi_0 = 0$) and a horizontally loaded shell ($\varphi_0 = \pi/2$), as the vibroacoustic behavior of a shell in a waveguide is dependent on the force direction. It is seen that there are more fluctuations present in the vertically loaded shell, and as such convergence to the limiting case occurs at larger waveguide depths compared to a horizontally loaded shell. In terms of comparing the limiting cases, the sound pressure level at the far field is generally greater for a fluid domain with a seabed only compared to the unbounded sea and the unbounded sea being greater than a fluid domain with a free surface only. Generally, the near field of the shell is unaffected by the waveguide depth (i.e., $y \sim R$ m).

This analytical method developed here is computationally efficient and will allow for parametric studies to be performed very quickly, and to consider different scenarios for the underwater sound propagation by a forced cylindrical shell such as in a shallow waveguide, near a free surface, near a sea bed, unbounded sea, and intermediary configurations that have been noticed to demonstrate complex acoustic propagation to the far field.

## 4. Conclusions

An efficient analytical model for evaluating the shallow water vibroacoustics of a thin cylindrical shell under line-distributed harmonic excitation is herein presented. The waveguide implemented is formed by an upper free surface and a lower seabed. The analytical approach is developed using Flügge's shell equations, image source method and applying Graf's addition theorem to reconcile the different coordinate systems of the image sources. Indicators for the vibration, acoustic pressure, and radiated sound power are presented and verified against corresponding FEM simulation results, showing excellent agreement. The present analytical model reduces the computational complexity of the vibroacoustic problem. Typically to solve for a far point, the computational domain for the COMSOL model is required to be extended, increasing the number of computations required to solve the system. However, the analytical approach does not encounter the same limitation. It is also several orders of magnitude faster in computation for evaluating the acoustic pressure at a single observation point in the fluid domain across a wide frequency range, requiring less memory and data storage necessary for the computation compared to FEM simulations.

Subsequent investigations involved using the present method to investigate the standing waves criterion, the importance of including the image source contributions in the fluid-structure coupling by comparison of results against the so-called "mirror effect" model, a comparison against a pulsating monopole, and finally, limiting cases of different waveguide configurations. It is recognized that the present method is a more accurate approach than the typical "mirror" effect method which neglects the image source contribution in the fluid-structure coupling term. The comparison is shown to be similar for predicting the structural response and different for the acoustic response, especially at the low frequencies and standing wave frequencies. It emphasizes that the "mirror" effect is not suitable for predicting acoustic outputs. The oscillations observed on the curves for the pressure level in function of the horizontal distance from the shell are a direct consequence of the image source contributions, which are affected by the force configuration. A vertically loaded shell will exhibit oscillations even at low frequencies, while radiation from a horizontally loaded shell is similar to a pulsating monopole except at standing wave frequencies. For observing the acoustic response in different waveguide configurations, the general conclusions are that the seabed increases the acoustic pressure in the far field whereas the free surface decreases the acoustic pressure in the far field relative to an unbounded sea case. A larger waveguide is necessary for a vertically loaded shell before the oscillations can be ignored, and the limiting case can be assumed, relative to a horizontally loaded shell. Finally, the vertically loaded shell behaves different to a horizontally loaded shell, while a horizontally loaded shell is similar to a pulsating monopole.

It is believed that the simplified modeling framework employed in this study (thin shell model, two dimensional approximation, perfect underwater waveguide) being numerically verified can provide valuable insight in more complex vibroacoustic phenomena and can be used as a benchmark and verification tool for future operational models.

## Acknowledgements

The first author acknowledges that this research is supported by an Australian Government Research Training Program Scholarship. The second author gratefully acknowledges the financial support by the Australian Government through the Australian Research Councils Discovery Early Career Project funding scheme (project DE190101412).

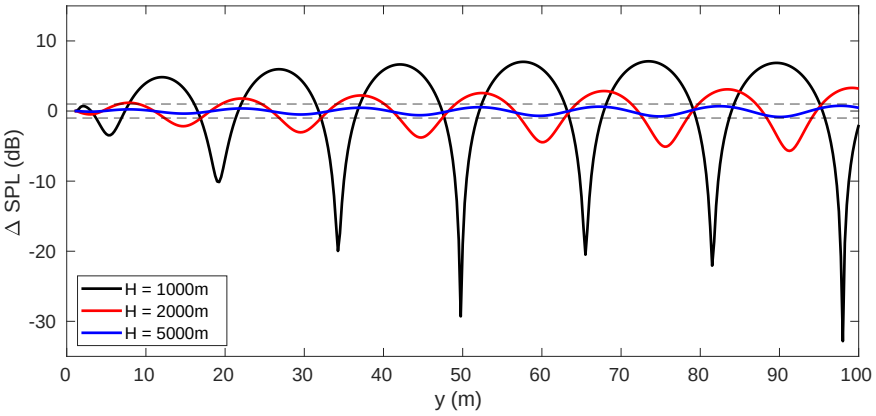


(a) 100 Hz

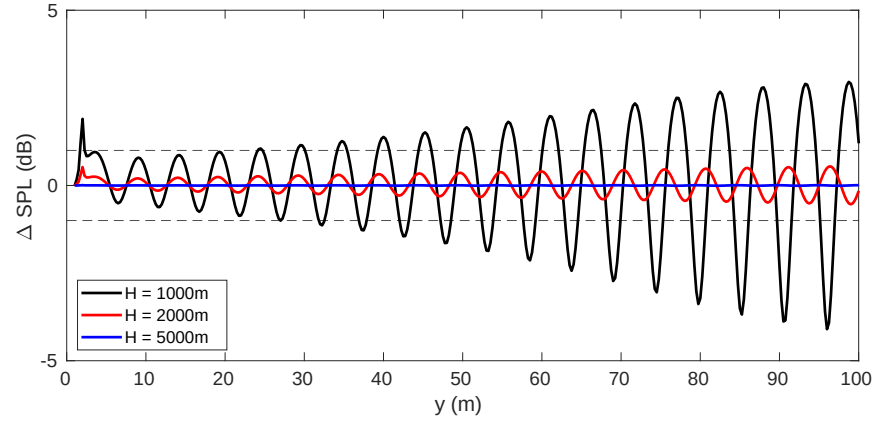


(b) 300 Hz

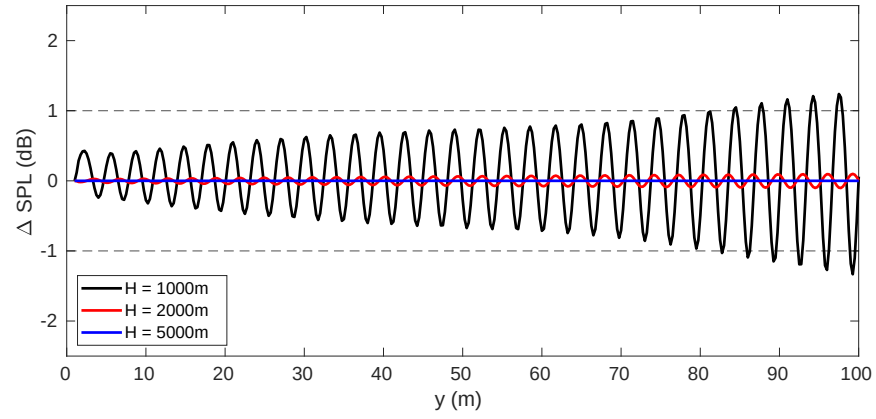


(c) 500 Hz

**Figure 14:** Difference in sound pressure level (SPL) between a vertically loaded shell positioned at the midpoint of large waveguides, and in an unbounded fluid domain.

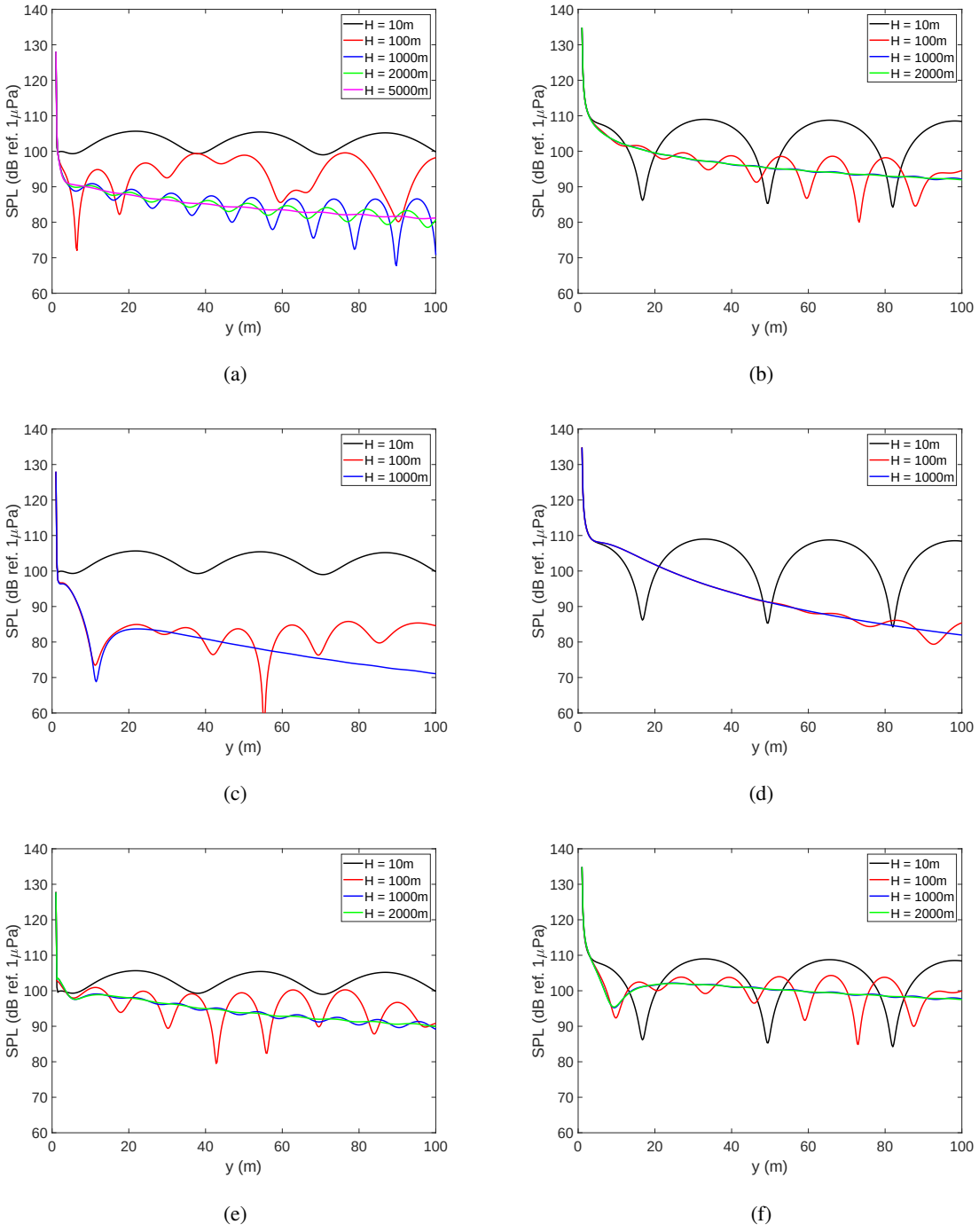


**Figure 15:** Convergence of (a,c,e) vertically loaded shell and (b,d,f) horizontally loaded shell for different waveguide configurations: (a,b) increasing and equally distant from the free surface and seabed, (c,d) with increasing distances of the free surface, and (e,f) with increasing distances of the seabed and at 150 Hz.

## CRediT authorship contribution statement

**Jamie Kha:** Conceptualization, Methodology, Investigation, Validation, Formal analysis, Software, Writing - original draft. **Mahmoud Karimi:** Conceptualization, Software, Validation, Formal analysis, Writing - review & editing, Funding acquisition, Supervision, Project administration. **Laurent Maxit:** Conceptualization, Formal analysis, Writing - review & editing, Supervision. **Alex Skvortsov:** Writing - review & editing, Funding acquisition, Supervision. **Ray Kirby:** Writing - review & editing, Supervision.

## References


Chen, L., Liang, X., Yi, H., 2016. Vibro-acoustic characteristics of cylindrical shells with complex acoustic boundary conditions. Ocean Eng. 126, 12–21. doi:10.1016/j.oceaneng.2016.08.028.

Ergin, A., Temarel, P., 2002. Free vibration of a partially liquid-filled and submerged, horizontal cylindrical shell. J. Sound Vib. 254, 951–965. doi:10.1006/jsvi.2001.4139.

Guo, W., Li, T., Zhu, X., Miao, Y., 2018. Sound-structure interaction analysis of an infinite-long cylindrical shell submerged in a quarter water domain and subject to a line-distributed harmonic excitation. J. Sound Vib. 422, 48–61. doi:10.1016/j.jsv.2018.02.031.

Guo, W., Li, T., Zhu, X., Miao, Y., Zhang, G., 2017. Vibration and acoustic radiation of a finite cylindrical shell submerged at finite depth from the free surface. J. Sound Vib. 393, 338–352. doi:10.1016/j.jsv.2017.01.003.

Guo, Y.P., 1996. Acoustic scattering from cylindrical shells with deck-type internal plate at oblique incidence. J. Acoust. Soc. Am. 99, 2701–2713. doi:10.1121/1.414812.

Hasheminejad, S., Azarpeyvand, M., 2004. Modal vibrations of a cylindrical radiator over an impedance plane. J. Sound Vib. 278, 461–477. doi:10.1016/j.jsv.2003.10.039.

Hasheminejad, S.M., Azarpeyvand, M., 2003. Modal vibrations of an infinite cylinder in an acoustic halfspace. Int. J. Eng. Sci. 41, 2253–2271. doi:10.1016/S0020-7225(03)00214-3.

Jiang, L., Zou, M., Huang, H., Feng, X., 2018. Integrated calculation method of acoustic radiation and propagation for floating bodies in shallow water. J. Acoust. Soc. Am. 143, EL430–EL436. doi:10.1121/1.5039415.

Junger, M.C., Feit, D., 1986. Sound, Structures, and their Interaction. MIT Press.

Kerferd, B., Eggler, D., Karimi, M., Kessissoglou, N., 2020. Active acoustic cloaking of cylindrical shells in low Mach number flow. J. Sound Vib. 479, 115400. URL: https://linkinghub.elsevier.com/retrieve/pii/S0022460X20302327, doi:10.1016/j.jsv.2020.115400.

Kha, J., Karimi, M., Maxit, L., Skvortsov, A., Kirby, R., 2022. An analytical approach for modelling the vibroacoustic behavior of a heavy fluid-loaded plate near a free surface. J. Sound Vib. , 117206URL: https://linkinghub.elsevier.com/retrieve/pii/S0022460X22003996, doi:10.1016/j.jsv.2022.117206.

Lee, W.M., Chen, J.T., 2010. Scattering of flexural wave in a thin plate with multiple circular holes by using the multipole Trefftz method. Int. J. Solids Struct. 47, 1118–1129. doi:10.1016/j.ijsolstr.2009.12.002.

Leissa, A.W., 1993. Vibration of shells. American Institute of Physics.

Li, H., Wu, C., Huang, X., 2003. Parametric study on sound radiation from an infinite fluid-filled/semi-submerged cylindrical shell. Appl. Acoust. 64, 495–509. doi:10.1016/S0003-682X(02)00125-1.

Li, T.Y., Miao, Y.Y., Ye, W.B., Zhu, X., Zhu, X.M., 2014. Far-field sound radiation of a submerged cylindrical shell at finite depth from the free surface. J. Acoust. Soc. Am. 136, 1054–1064. doi:10.1121/1.4890638.

Linton, C.M., 1998. The Green's Function for the Two-Dimensional Helmholtz Equation in Periodic Domains. J. Eng. Math. 33, 377–401. doi:10.1023/A:1004377501747.

Liu, Z.z., Li, T.y., Zhu, X., Zhang, J.j., 2010. The effect of hydrostatic pressure fields on the dispersion characteristics of fluid-shell coupled system. J. Mar. Sci. Eng. 9, 129–136. doi:10.1007/s11804-010-9010-3.

Marsick, A., Sharma, G.S., Eggler, D., Maxit, L., Meyer, V., Kessissoglou, N., 2021. On the vibro-acoustic response of a cylindrical shell submerged near a free sea surface. J. Sound Vib. 511, 116359. doi:10.1016/j.jsv.2021.116359.

Maxit, L., Ginoux, J.M., 2010. Prediction of the vibro-acoustic behavior of a submerged shell non periodically stiffened by internal frames. J. Acoust. Soc. Am. 128, 137–151. doi:10.1121/1.3436526.

Maxit, L., Guasch, O., Meyer, V., Karimi, M., 2020a. Noise radiated from a periodically stiffened cylindrical shell excited by a turbulent boundary layer. J. Sound Vib. 466, 115016. doi:10.1016/j.jsv.2019.115016.

Maxit, L., Karimi, M., Meyer, V., Kessissoglou, N., 2020b. Vibroacoustic responses of a heavy fluid loaded cylindrical shell excited by a turbulent boundary layer. J. Fluids Struct. 92, 102758. doi:10.1016/j.jfluidstructs.2019.102758.

Pathak, A.G., Stepanishen, P.R., 1994. Acoustic harmonic radiation from fluid-loaded infinite cylindrical elastic shells using elasticity theory. J. Acoust. Soc. Am. 96, 573–582. doi:10.1121/1.410443.

Qatu, M.S., 2002. Recent research advances in the dynamic behavior of shells: 1989–2000, Part 2: Homogeneous shells. Appl. Mech. Rev. 55, 415–434. doi:10.1115/1.1483078.

Qian, Z., Shang, D., Xu, X., He, Y., Zhai, J., 2021. A semi-analytical method for the 3d elastic structural-acoustic radiation in shallow water. J. Theor. Comput. Acoust. 0, 2150011. doi:10.1142/S2591728521500110.

Salaün, P., 1991. Effect of a free surface on the far-field pressure radiated by a point-excited cylindrical shell. J. Acoust. Soc. Am. 90, 2173–2181. doi:10.1121/1.402373.

Wang, P., Li, T., Zhu, X., 2017. Free flexural vibration of a cylindrical shell horizontally immersed in shallow water using the wave propagation approach. Ocean Eng. 142, 280–291. doi:10.1016/j.oceaneng.2017.07.006.

Williams, E.G., 1999. Fourier acoustics: sound radiation and nearfield acoustical holography. Academic Press.

Williams, P., Kirby, R., Karimi, M., 2022. Sound power radiated from acoustically thick, fluid loaded, axisymmetric pipes excited by a central monopole. J. Sound Vib. 527, 116843. doi:10.1016/j.jsv.2022.116843.

Ye, W.B., Li, T.Y., Zhu, X., 2012. The Vibro-Acoustic Characteristics of the Cylindrical Shell Partially Submerged in the Fluid. Appl. Mech. Mater. 170-173, 2303–2311. doi:10.4028/www.scientific.net/AMM.170-173.2303.

Zhang, L., Duan, J.x., Da, L.l., Xu, G.j., Sun, X.h., 2020. Vibroacoustic radiation and propagation properties of slender cylindrical shell in uniform shallow sea. Ocean Eng. 195, 106659. doi:10.1016/j.oceaneng.2019.106659.

Zhao, K., Fan, J., Wang, B., Tang, W., 2020. Vibroacoustic behavior of a partially immersed cylindrical shell under point-force excitation: Analysis and experiment. Appl. Acoust. 161, 107170. doi:10.1016/j.apacoust.2019.107170.